

# ARMS ocean emissivity model application

Fuzhong Weng

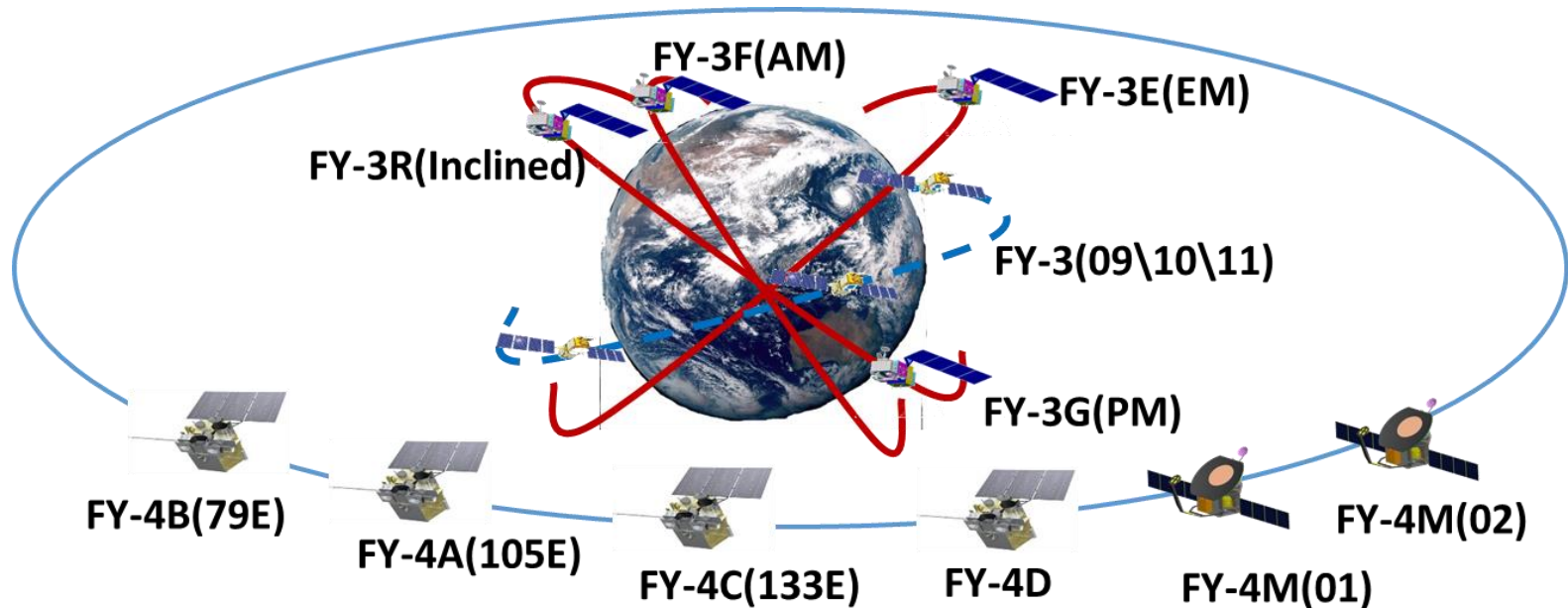
Laboratory of Severe Weather  
Chinese Academy of Meteorological Sciences

*A Reference Quality Model for Ocean Surface Emissivity and  
Backscatter from the Microwave to the Infrared  
Bern, Switzerland, November 21, 2019*

# Outline

- Highlights on FengYun satellite program
- ARMS microwave ocean emissivity models
- Simulations vs observations
- Effects of surface emissions vs antenna emission
- Summary and Conclusions

# Fengyun Meteorological Satellite by 2030

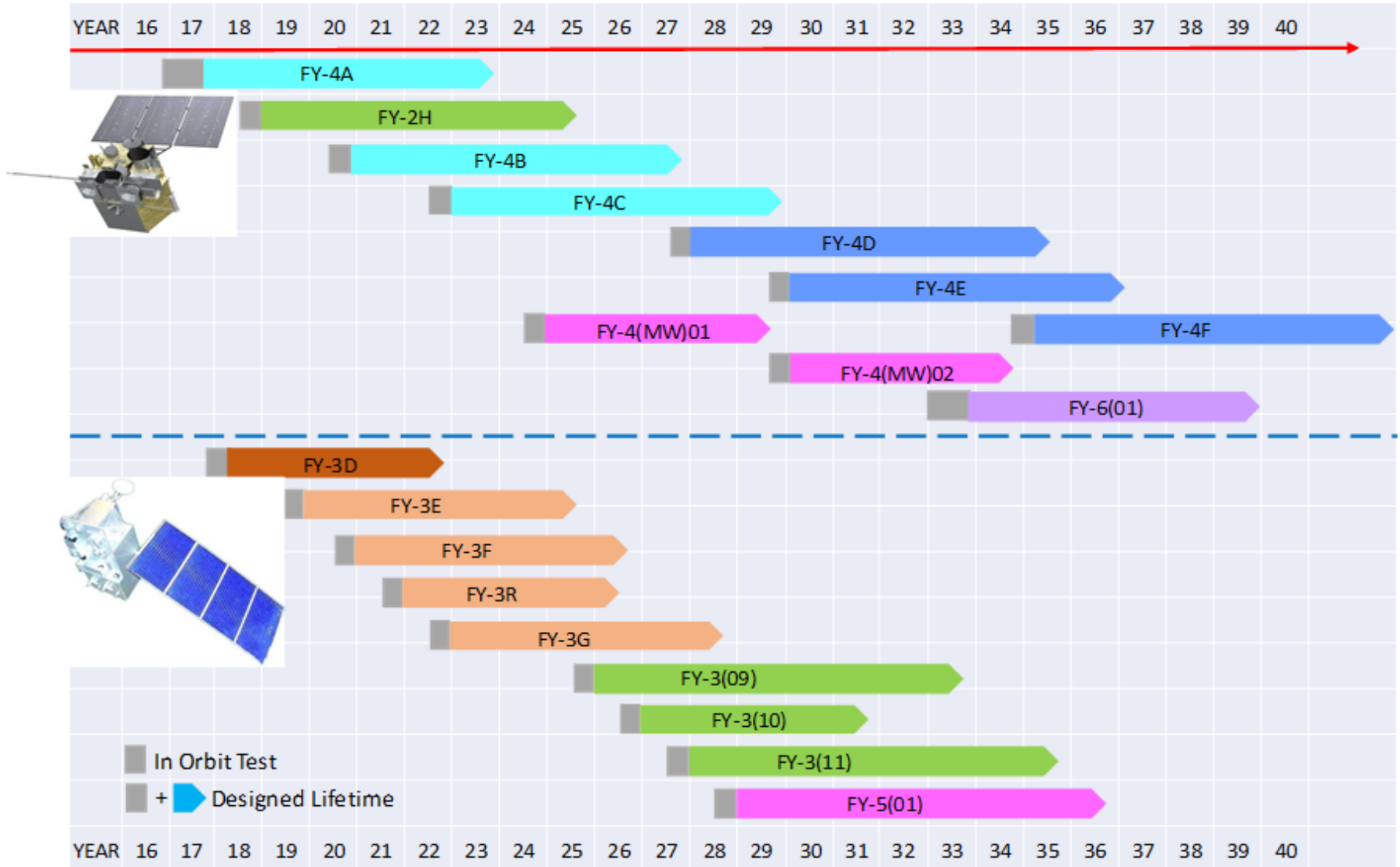


The LEO realizes the network of covering the EM, AM and PM satellite observation, and the time limit of global data updating has been raised from 6 hours to 3 hours. Fine detection of elements such as precipitation and greenhouse gas.

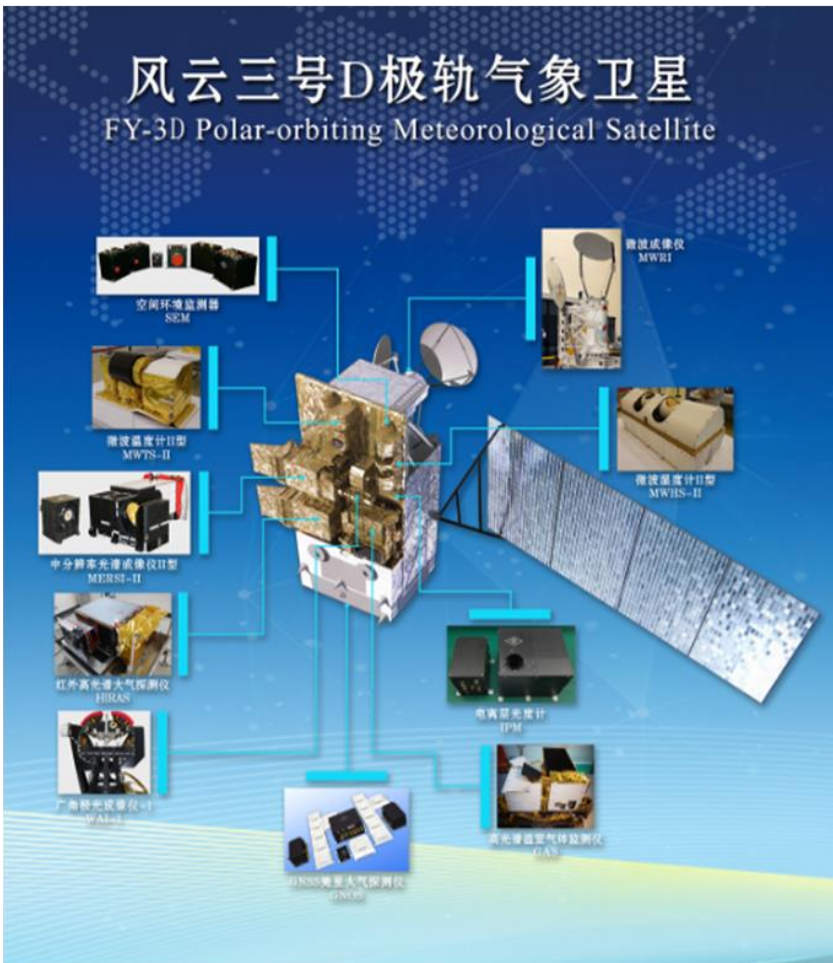
The new pattern of GEO observation: imaging, hyper-spectral and microwave sounding.

FY-4B: rapid scan(min), FY-4C: five minutes disk image, sounding abilities, whole disk lightning mapper.

# Fengyun Meteorological Satellite by 2040



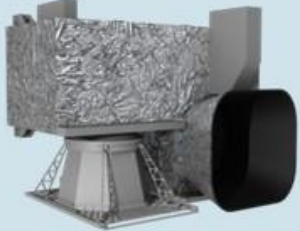
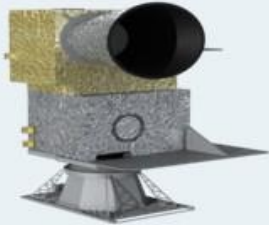


# FY-3D Polar-Orbiting Meteorological Satellite



Payload Name	Channel with Coverage	Numbers Spectral
MEDium Resolution Spectral Imager (MERSI-2)	25 (0.413 – 12 μm)	
Hyperspectral Atmospheric Sounder (HIRAS)	1370 (3.92 – 15.38 μm)	
MicroWave Radiation Imager (MWRI)	10 (10.65 – 89 GHz)	
MicroWave Temperature Sounder (MWTS-2)	13 (50.3 – 57.29 GHz)	
MicroWave Humidity Sounder (MWHs-2)	15 (89.0 – 183.31 GHz)	
GNSS Occultation Sounder (GNOS)	29 (–)	
Greenhouse-gases Absorption Spectrometer (GAS)	5540 (0.75 – 2.38 μm)	
Wide angle Aurora Imager (WAI)	1 (140 – 180 nm)	
Ionospheric PhotoMeter (IPM)	3 (130 – 180 nm)	
Space Environment Monitor (SEM)	25 (–)	

- Four brand new instruments added (HIRAS, GAS, WAI, IPM)
- One Successive instrument updated (MERSI-2)
- All the successive Instruments performance are improved significantly

# FY-4A Geostationary Satellite

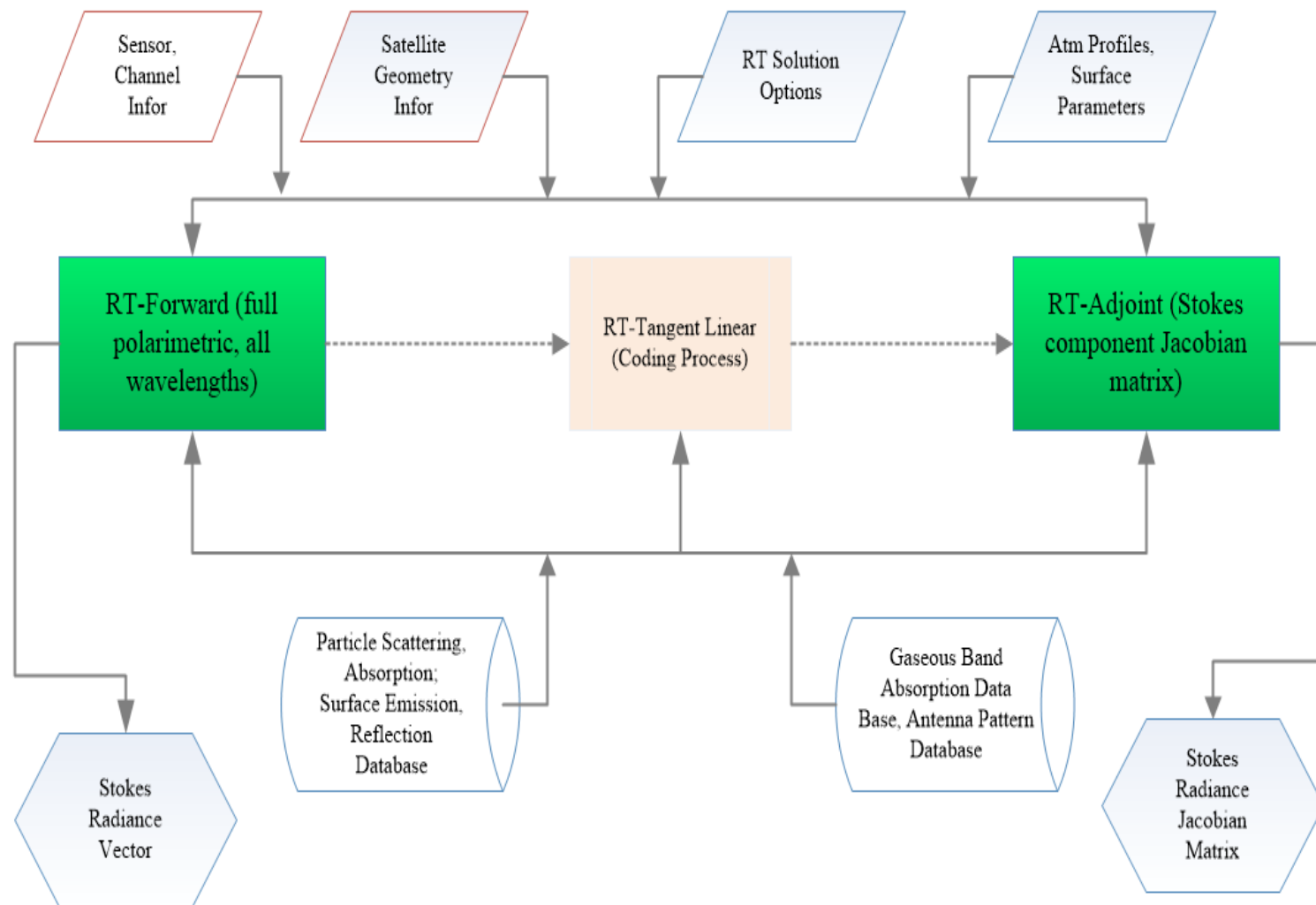
Instrument	Purposes	
 A 3D rendering of the AGRI instrument, showing a large, rectangular, metallic structure with a complex internal structure and a black cylindrical component on the right side.	<b>AGRI:</b> <i>Advanced Geosynchronous Radiation Imager</i>	14 -channel Earth images
 A 3D rendering of the GIIRS instrument, showing a rectangular box with a large black cylindrical lens or aperture on the front and a smaller cylindrical component on the side.	<b>GIIRS:</b> <i>Geostationary Interferometric InfraRed Sounder</i>	Clear-sky atmospheric temperature and humidity profiles
 A 3D rendering of the LMI instrument, showing two large, cylindrical, metallic structures with a textured surface, mounted on a common base.	<b>LMI:</b> <i>Lightning Mapping Imager</i>	Lightning distribution map in China area
 A circular inset containing three small images of electronic components, likely part of the SEP instrument, showing various circuit boards and modules.	<b>SEP:</b> <i>Space Environment Package</i>	Space electric and magnetic environment information



# Unique Aspects in FY Satellite Missions

- In its leo program, the operational satellite missions are often carrying some advanced instruments for new exploring the new sciences
- In geo and leo orbits, both high spectral IR and MW sounders are on board and allow for profiling atmospheric temperature and moisture under all weather conditions
- Both active and passive microwave instruments are deployed and allow for better profiling cloud and precipitation from operational missions
- Microwave imagers are flying on board FY satellites in both morning and afternoon orbits
- The missions in general provide critical supports to weather and climate applications as well as ecological and environment monitoring and assessments

# Advanced Radiative Transfer Modeling System (ARMS)





# ARMS Supported Instruments

- FY-3A MWTS
- FY-3A MWHS
- FY-3B MWTS
- FY-3B MWHS
- FY-3C MWTS-2
- FY-3C-MWHS-2
- FY-3D MWTS-2
- FY-3D MWHS-2
- FY-3 B/C/D MWRI
- FY-3 B/C VIRR
- FY-3C MERSI
- FY-3C IRAS
- FY-3D MERSI-2
- FY-3D HIRAS
- FY-4A GIIRS
- FY-4A AGRI
- FY-4M GMIS
- NOAA 15 to 19 AMSU-A
- NOAA 18-19 MHS
- NOAA 18-19 HIRS
- NOAA 15-19 AVHRR
- SNPP/NOAA-20 ATMS
- SNPP/NOAA-20 CrIS
- SNPP/NOAA-20 VIIRS
- METOP-A to C IASI
- METOP-A to C IASI
- METOP-A to C AMSU-A
- METOP-A to C AVHRR
- JAXA AMSR2
- NASA GMI
- EOS Aqua AIRS
- EOS Terra/Aqua MODIS

# ARMS Solvers

- Polarization Two-Stream Approximation (P2S)
- Advanced Doubling and Adding (ADA)
- Vector Doubling and Adding (VDA)
- DIScrete Ordinate Radiative Transfer (DISORT)
- Vector DIScrete Ordinate Radiative Transfer (VDISORT)

# Definition of Radiative Transfer Model

$$\mu \frac{d\mathbf{I}(\tau, \mu, \phi)}{d\tau} = -\mathbf{I}(\tau, \mu, \phi) + \mathbf{J}(\tau, \mu, \phi) + \mathbf{S}(\tau, \mu, \phi, \mu_0, \phi_0)$$

Extinction

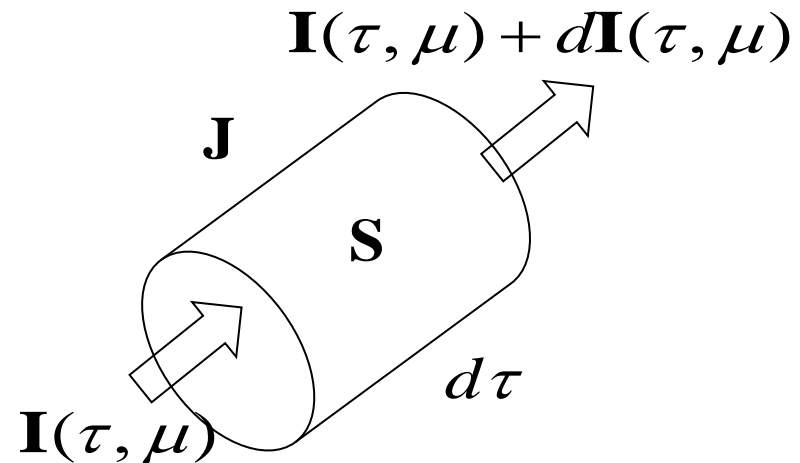
Multiple scattering

Source: single scattering & thermal emission

$$\mathbf{I} = [I, Q, U, V]$$

or

$$\mathbf{I} = [I_r, I_l, U, V]$$



# Source Terms and Multiple Scattering

Phase matrix



$$\mathbf{J} = \frac{\omega(\tau)}{4\pi} \int_0^{2\pi} \int_{-1}^1 \mathbf{M}(\tau, \mu, \phi; \mu', \phi') \mathbf{I}(\tau, \mu', \phi') d\mu' d\phi'$$

$$\mathbf{S}(\tau, \mu, \phi, \mu_0, \phi_0) = (1 - \omega) B \begin{pmatrix} 1 \\ 0 \\ 0 \\ 0 \end{pmatrix} + \frac{\omega F_0}{4\pi} \exp(-\tau / \mu_0) \begin{pmatrix} M_{11}(\phi, \mu_0, \phi_0) \\ M_{12}(\phi, \mu_0, \phi_0) \\ M_{13}(\phi, \mu_0, \phi_0) \\ M_{14}(\phi, \mu_0, \phi_0) \end{pmatrix}$$

# Radiative Transfer Solvers

- Discrete Ordinate Radiative Transfer (DISORT)
- Vector DISORT (VDISORT)
- Vector Double and Adding (VDA)
- Vector Matrix Operator (MO)
- Polarization Two Stream Approximation

# ARMS Atmospheric Optics

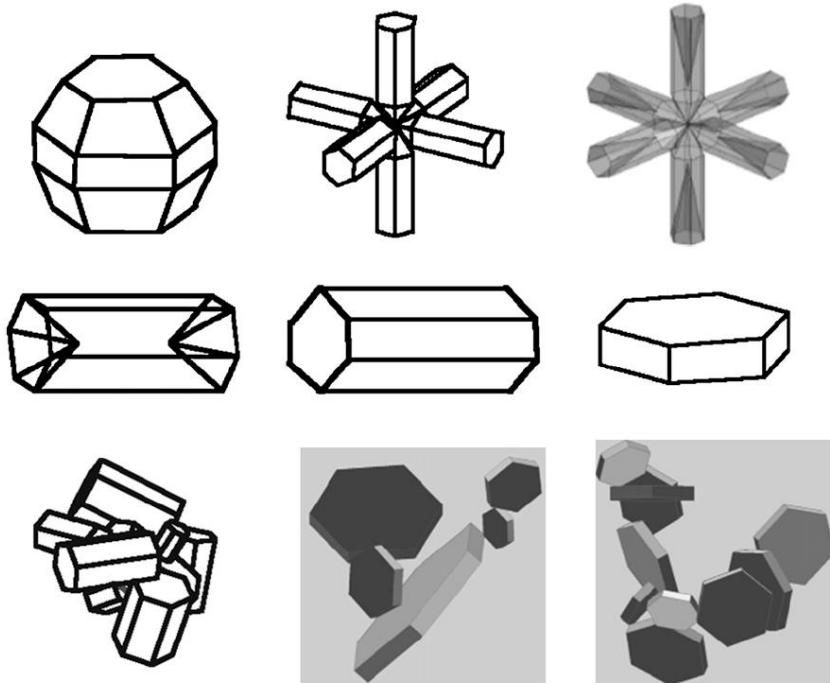
- Fast atmospheric gaseous absorption models trained by LBLRTM
- Cloud and aerosol particle scattering LUT generated from Mie
- Cloud and aerosol particle scattering LUT from T-Matrix

# Cloud Optical Property Library

## Ice particle single-scattering property database

Spectrally Consistent Scattering, Absorption, and Polarization Properties of Atmospheric Ice Crystals at Wavelengths from 0.2 to 100  $\mu\text{m}$

PING YANG,\* LEI BI,\* BRYAN A. BAUM,+ KUO-NAN LIU,# GEORGE W. KATTAWAR,@  
MICHAEL I. MISHCHENKO,& AND BENJAMIN COLE\*



- Developed with the most accurate and state-of-the-art light scattering computation methods (T-Matrix [Bi et al., 2014] and IGOM [Yang et al., 1996]);
- Wide coverage of the spectrum from 0.2 to 100  $\mu\text{m}$ ;
- Wide particle size range (maximum dimension) from 2~10<sup>4</sup>  $\mu\text{m}$ ;
- Complete scattering phase matrix with polarization
- Three degrees of ice surface roughness: Completely Smooth, Moderately Rough, Severely Rough;
- Extended to the microwave spectrum; temperature dependence considered;



# Spectral Bulk Scattering Properties of Ice Clouds

$$r_{eff} = \frac{3 \int_{r_{min}}^{r_{max}} V(r)n(r)dr}{2 \int_{r_{min}}^{r_{max}} A(r)n(r)dr},$$

Ice bulk optical properties as functions of effective radius  $R_{eff}$

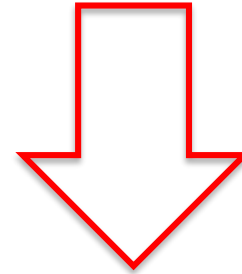
$$\overline{Q_{ext}} = \frac{\int_{r_{min}}^{r_{max}} [Q_{ext}(r)A(r)n(r)]dr}{\int_{r_{min}}^{r_{max}} [A(r)n(r)]dr},$$

$$\overline{Q_{sca}} = \frac{\int_{r_{min}}^{r_{max}} [Q_{sca}(r)A(r)n(r)]dr}{\int_{r_{min}}^{r_{max}} [A(r)n(r)]dr},$$

$$\overline{\omega} = \frac{\overline{Q_{sca}}}{\overline{Q_{ext}}},$$

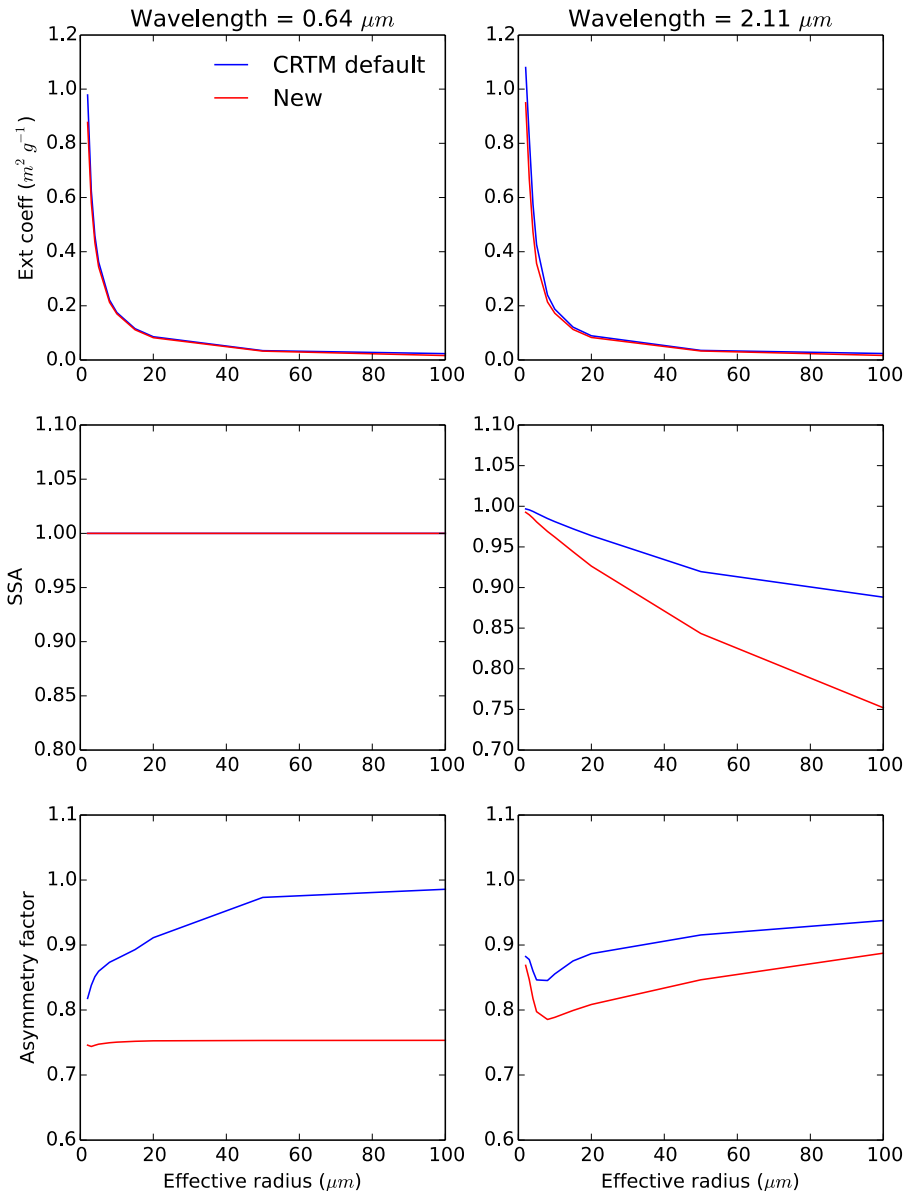
$$\overline{g} = \frac{\int_{r_{min}}^{r_{max}} [g(r)A(r)Q_{sca}(r)n(r)]dr}{\int_{r_{min}}^{r_{max}} [Q_{sca}(r)A(r)n(r)]dr},$$

$$\overline{P(\theta)} = \frac{\int_{r_{min}}^{r_{max}} [P(\theta,r)Q_{sca}(r)A(r)n(r)]dr}{\int_{r_{min}}^{r_{max}} [Q_{sca}(r)A(r)n(r)]dr},$$



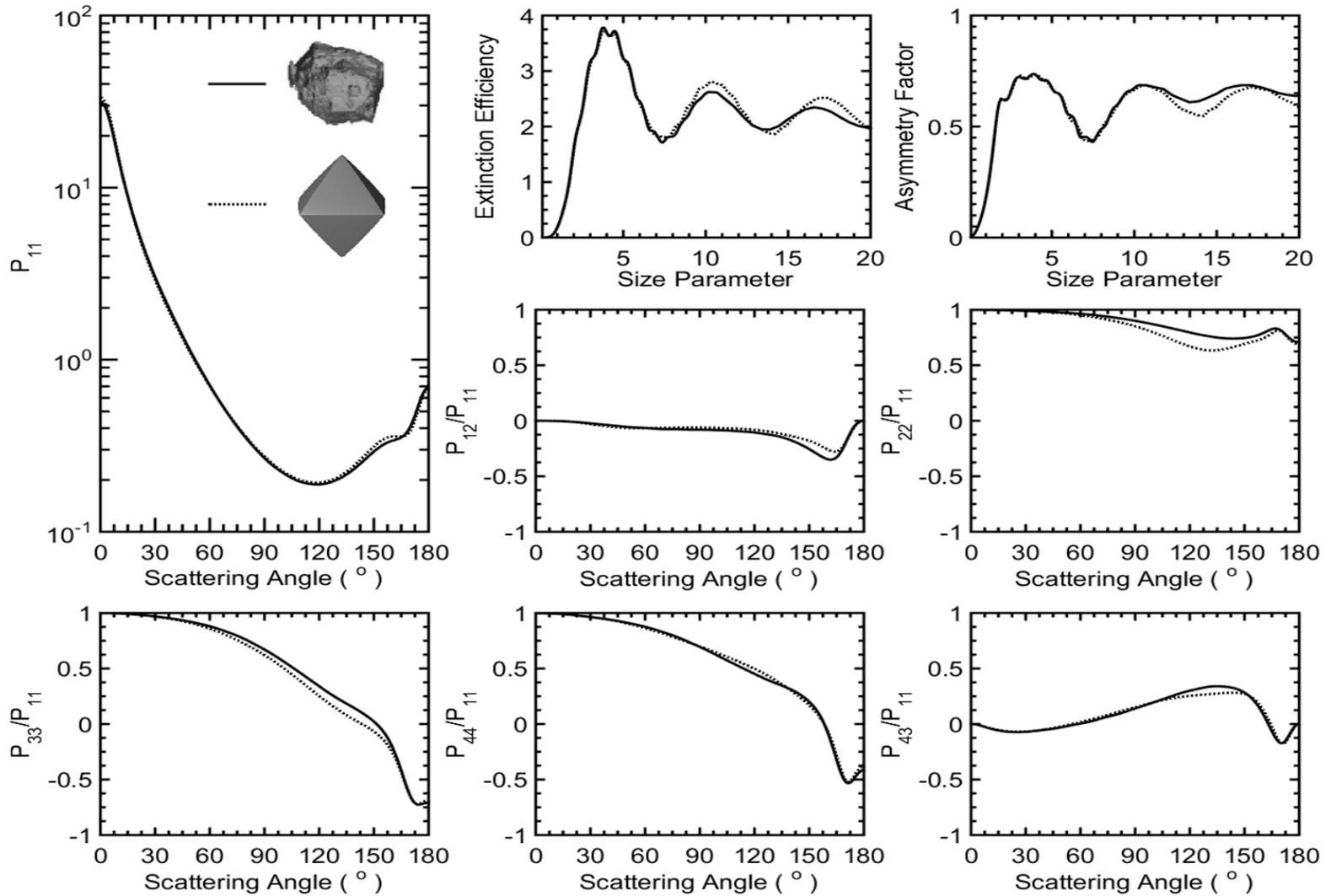
- Mass extinction coefficient
- Single-scattering albedo
- Asymmetry parameter
- Phase function Legendre expansion coefficient

# Ice Cloud Scattering Properties



- Ice mass extinction coefficients:
  - Little difference
- The single-scattering albedo:
  - $\sim 1$  (0.64  $\mu\text{m}$  wavelength)
  - Decreases with the increase of effective radius (2.11  $\mu\text{m}$  wavelength)
- The asymmetry factor:
  - Shortwave (0.64  $\mu\text{m}$ ) ice cloud is almost independent to the effective size and remains constant around 0.75.
  - Conversely, the CRTM default ice cloud asymmetry factor has increasingly larger value with an increase in the effective radius.

# Aerosol Scattering Database



# ARMS Surface Optics

- IR Ocean EM
  - Wu-Smith-IR
- MW Ocean EM
  - HSKS-EM
  - FASTEM
- MW Land EM
  - Advanced integral equation model (AIEM)
  - Two stream analytic model
- Data Bases
  - CNRW MW
  - TELSEM MW
  - UW IREMIS
  - CAMEL IR

# HSKS-Ocean Emissivity Model

## (Hollinger-Stogryn-Klein and Swift)

- A rough surface without foam coverage: Hollinger, J. P., 1971, Passive microwave measurements of sea surface roughness, IEEE Trans on Geosci. Elec., GE-9, 165-169.
- Foam Reflectivity: Stogryn, A. 1972, A study of radiometric emission from a rough sea surface, NASA contractor report NASA, CR-2088.
- Calm water reflectivity: Klein and Swift, (1977 " emissivity for calm water" IEEE Trans. Antennas Propag., 25, 104-111.

# HSKS-Ocean Emissivity Model

$$\Gamma_p = (1 - f_c) \Gamma_{p, foam-free} + f_c \Gamma_{p, foam}$$

Foam-free Reflectivity in H-Polarization due to wind roughness

$$tr = w(1.15 \times 10^{-1} + 3.8 \times 10^{-5} \times \theta^2) \sqrt{f \times 10^{-9}}$$

$$\Gamma_{h, foam-free} = \Gamma_{h, calm} - tr / t_s$$

Foam-free Reflectivity in V-Polarization due to wind roughness

$$tr = w(1.17 \times 10^{-1} - 2.09 \times 10^{-3} \times \exp(7.32 \times 10^{-2} \times \theta)) \sqrt{f \times 10^{-9}}$$

$$\Gamma_{v, foam-free} = \Gamma_{v, calm} - tr / t_s$$

Foam Reflectivity in H-Polarization

$$g = 1.0 - 1.748 \times 10^{-3} \theta - 7.336 \times 10^{-5} \times \theta^2 + 1.044 \times 10^{-7} \times \theta^3$$

$$\Gamma_{h, foam} = 1.0 - (208.0 + 1.29 \times 10^{-9} * f) / (t_s g)$$

Foam Reflectivity in V-Polarization

$$g = 1.0 - 9.946 \times 10^{-4} \times \theta + 3.218 \times 10^{-5} \times \theta^2 - 1.187 \times 10^{-6} \times \theta^3 + 7 \times 10^{-20} \times \theta^{10}$$

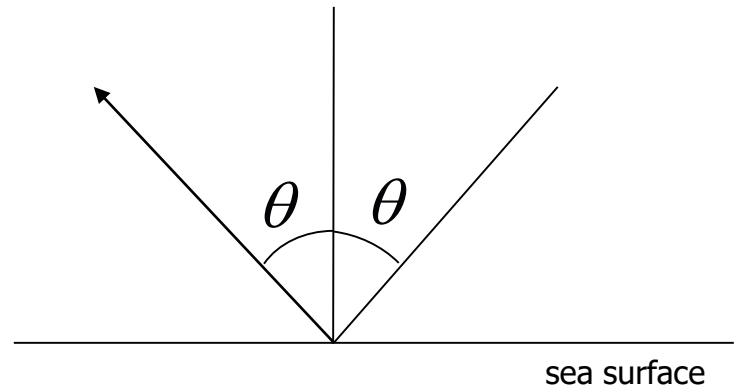
$$\Gamma_{v, foam} = 1.0 - (208.0 + 1.29 \times 10^{-9} * f) / (t_s g)$$

# Refractivity or Emissivity for Calm Water Surface

For a specular surface, reflectivity can be calculated by Fresnel law:

$$\Gamma_{v,calm} = \frac{\varepsilon(f, \theta) \cos \theta - \sqrt{\varepsilon(f, \theta) - \sin^2 \theta}}{\varepsilon(f, \theta) \cos \theta + \sqrt{\varepsilon(f, \theta) - \sin^2 \theta}}$$

$$\Gamma_{h,calm} = \frac{\cos \theta - \sqrt{\varepsilon(f, \theta) - \sin^2 \theta}}{\cos \theta + \sqrt{\varepsilon(f, \theta) - \sin^2 \theta}}$$



$\Gamma_p(f, \theta)$  Reflectivity       $f$  Frequency       $\theta$  Local zenith angle



# Foam Coverage

Foam is a mixture of air and water and has a higher emissivity than flat water

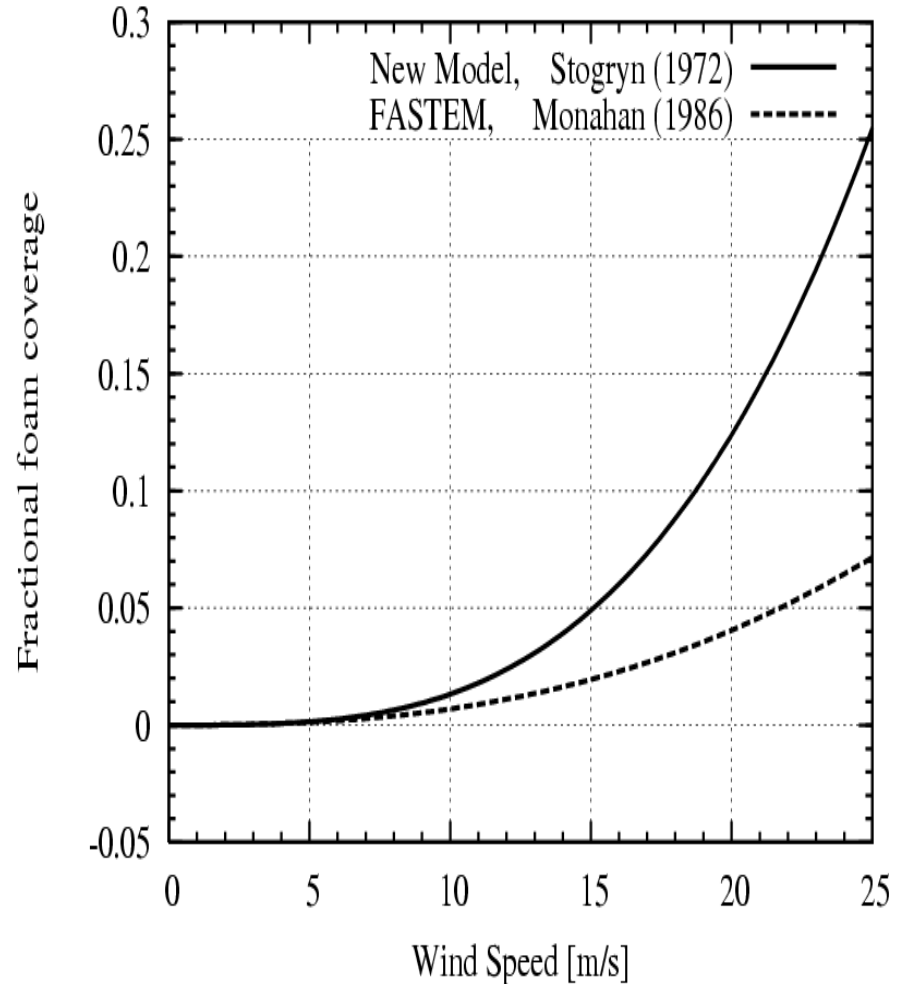
Foam coverage:

Stogryn, 1972

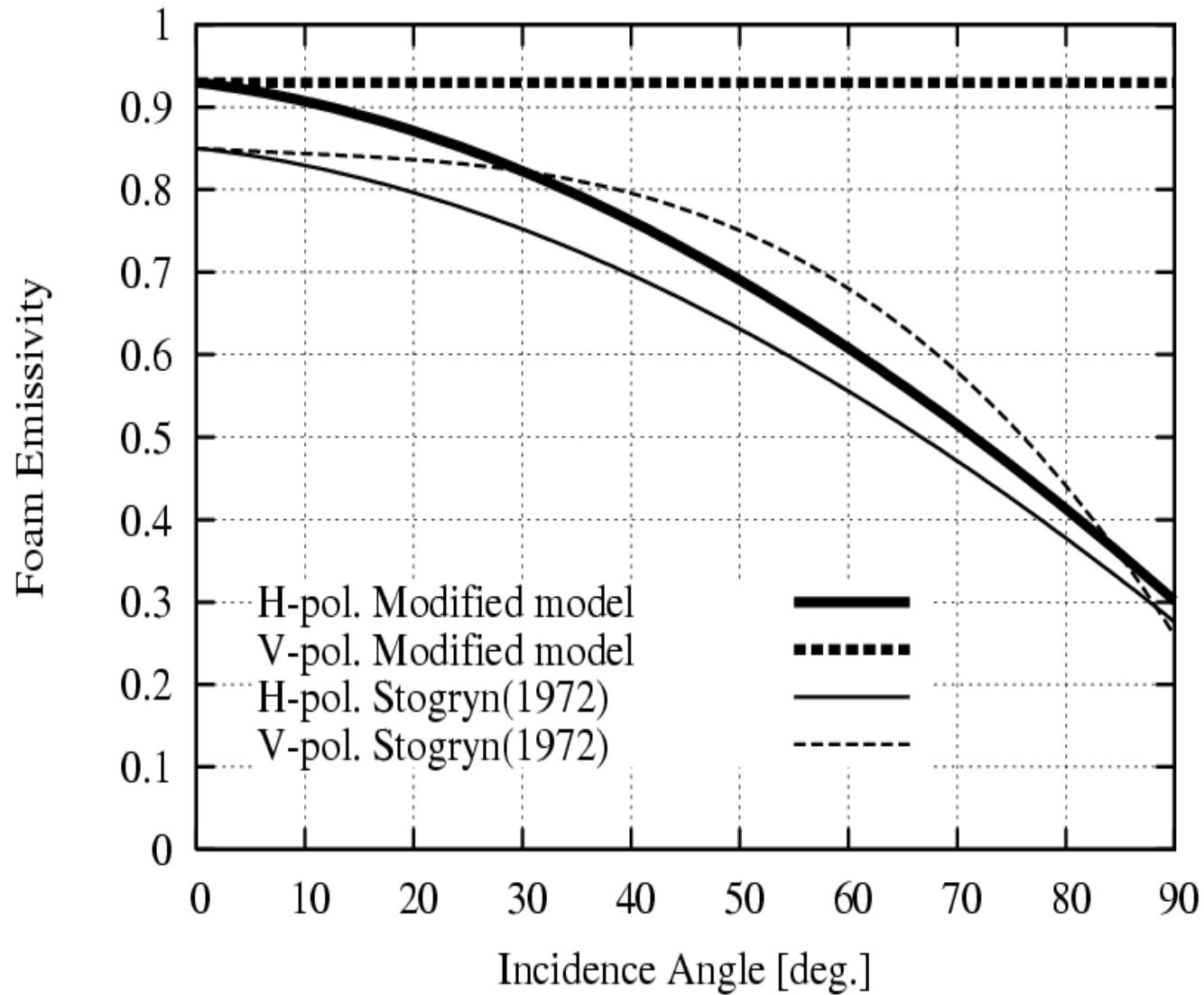
$$f_c = 7.75 \times 10^{-6} \left( \frac{V}{V_0} \right)^{3.231}$$

Monahan, 1986

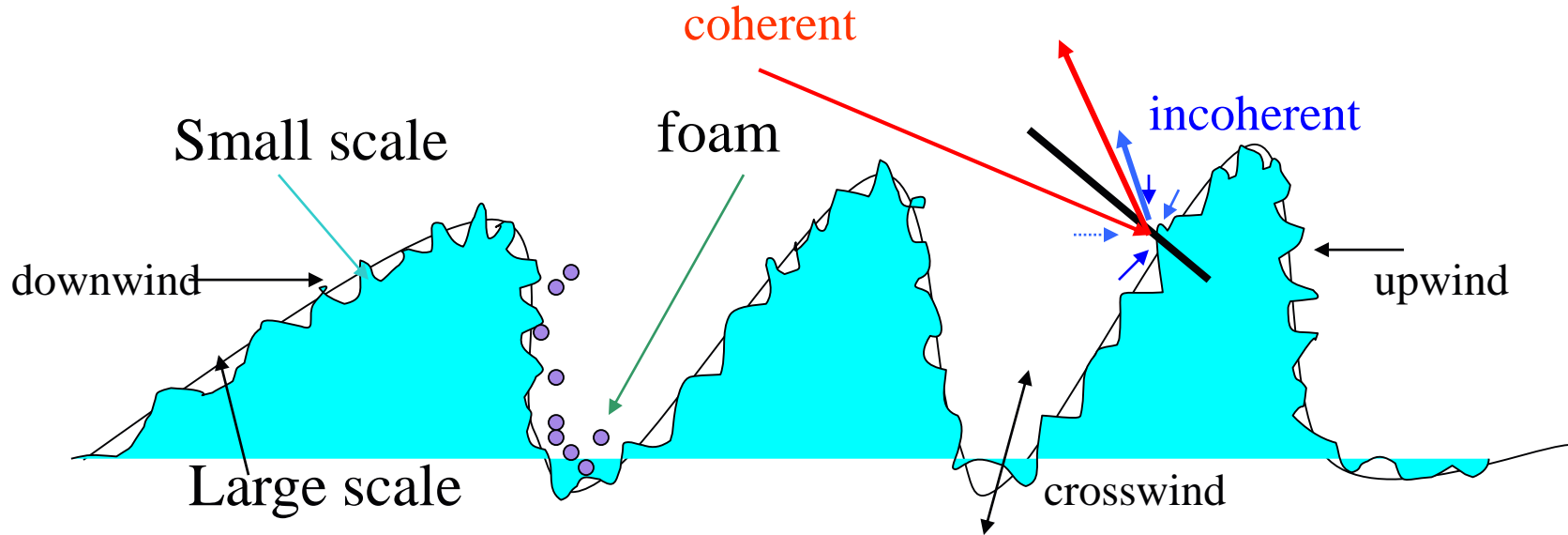
$$f_c = 1.95 \times 10^{-5} u^{2.55}$$



# Foam Emissivity vs. Angle



# Two-Scale Ocean Emissivity Model



The large-scale roughness is dependent on the gravity waves and whereas the small irregularities is affected by capillary waves. There are coherent reflection and incoherent scattering associated with the waves in both scales

# Surface MW BRDF Emissivity Model

## Relationship of BRDF, Bistatic Coeffs and Emissivity

$$\begin{aligned}
 e_p(\vartheta_i, \varphi_i) &= 1 - r_p(\vartheta_i, \varphi_i) \\
 r_p(\vartheta_i, \varphi_i) &= \frac{1}{4\pi} \int_0^{2\pi} \int_0^{\pi/2} (\sigma_{pp}(\vartheta_s, \varphi_s; \vartheta_i, \varphi_i) + \sigma_{qp}(\vartheta_s, \varphi_s; \vartheta_i, \varphi_i)) \frac{\sin\vartheta_s}{\cos\vartheta_i} d\vartheta_s d\varphi_s \\
 &= \int_0^{2\pi} \int_0^{\pi/2} (\gamma_{pp}(\vartheta_s, \varphi_s; \vartheta_i, \varphi_i) + (\gamma_{qp}(\vartheta_s, \varphi_s; \vartheta_i, \varphi_i)) \sin\vartheta_s) d\vartheta_s d\varphi_s \\
 &= r_p^{coherent}(\vartheta_i, \varphi_i) + r_p^{incoherent}(\vartheta_i, \varphi_i)
 \end{aligned}$$

where  $p, q$  stands for polarization,  $s$  for scattering,  $i$  for incident

$$I_{stokes} = \begin{bmatrix} \langle |E_h|^2 \rangle \\ \langle |E_v|^2 \rangle \\ 2\text{Re}\langle E_v E_h^* \rangle \\ 2\text{Im}\langle E_v E_h^* \rangle \end{bmatrix} = c \begin{bmatrix} T_h \\ T_v \\ U \\ V \end{bmatrix}$$

$$\begin{bmatrix} r_h(\vartheta_i, \varphi_i) \\ r_v(\vartheta_i, \varphi_i) \\ r_U(\vartheta_i, \varphi_i) \\ r_V(\vartheta_i, \varphi_i) \end{bmatrix}^{coh} = \begin{bmatrix} |R_{hh}^{(0)}|^2 + 2\text{Re}(R_{hh}^{(0)} R_{hh}^{(2)*}) \\ |R_{vv}^{(0)}|^2 + 2\text{Re}(R_{vv}^{(0)} R_{vv}^{(2)*}) \\ 2\text{Re}(R_{hh}^{(0)*} R_{vh}^{(2)} + R_{vv}^{(0)} R_{hv}^{(2)*}) \\ 2\text{Im}(R_{hh}^{(0)*} R_{vh}^{(2)} + R_{vv}^{(0)} R_{hv}^{(2)*}) \end{bmatrix} \text{Yueh, 1997}$$

$$\begin{bmatrix} r_h(\vartheta_i, \varphi_i) \\ r_v(\vartheta_i, \varphi_i) \\ r_U(\vartheta_i, \varphi_i) \\ r_V(\vartheta_i, \varphi_i) \end{bmatrix}^{inc} = \int_0^{2\pi} \int_0^{\pi/2} \begin{bmatrix} R_{hh}^{(1)} R_{hh}^{(1)*} + R_{hv}^{(1)} R_{hv}^{(1)*} \\ R_{vv}^{(1)} R_{vv}^{(1)*} + R_{vh}^{(1)} R_{vh}^{(1)*} \\ 2\text{Re}(R_{vh}^{(1)} R_{hh}^{(1)*} + R_{vv}^{(1)} R_{hv}^{(1)*}) \\ 2\text{Im}(R_{vh}^{(1)} R_{hh}^{(1)*} + R_{vv}^{(1)} R_{hv}^{(1)*}) \end{bmatrix} \sin\vartheta_s d\vartheta_s d\varphi_s$$

where  $R_{pq}^0 = R_{pq}^0(\vartheta_s, \varphi_s; \vartheta_i, \varphi_i)$  are SPM bistatic coefficients

There are several well-established methods for simulation of electromagnetic scattering from randomly rough surfaces

❑ **Kirchhoff Method (KM)** based on the assumption that the wavelength of the incident wave is much shorter than the horizontal variations of the surface so that the general solution can be regarded as the integration of local plane-boundary reflections.

*Tangential Plane Approximation*

*Stationary Phase Approximation and Geometric Optics (GO) (FASTEM)*

*Scalar Approximation and Physical Optics (PO)*

❑ **Small Perturbation Method (SPM)** based on the assumption that the surface correlation length and its standard deviation are smaller than the wavelength (low frequencies).

❑ **Composite Two-scale Model** based on the separation of both the surface and the EM wave into two distinct scales, e.g., Yueh et al., 1997

# Water Permittivity Model

Debye (1929) model for pure water, the permittivity

$$\epsilon = \epsilon_{\infty} + \frac{\epsilon_s - \epsilon_{\infty}}{1 + j2\pi f\tau}$$

Dissolved salt in water will be a good conductor and contributes to imaginary part

$$\epsilon = \epsilon_{\infty} + \frac{\epsilon_s - \epsilon_{\infty}}{1 + j2\pi f\tau} + j \frac{\alpha}{2\pi f\epsilon_0}$$

For a better performance at higher frequency, it is found that double Debye is needed with

$$\epsilon = \epsilon_{\infty} + \frac{\epsilon_s - \epsilon_1}{1 + j2\pi f\tau_1} + \frac{\epsilon_1 - \epsilon_{\infty}}{1 + j2\pi f\tau_2} + j \frac{\alpha}{2\pi f\epsilon_0}$$

$\epsilon_1$  is the permittivity at an intermediate frequency

# Water Permittivity vs. Frequency

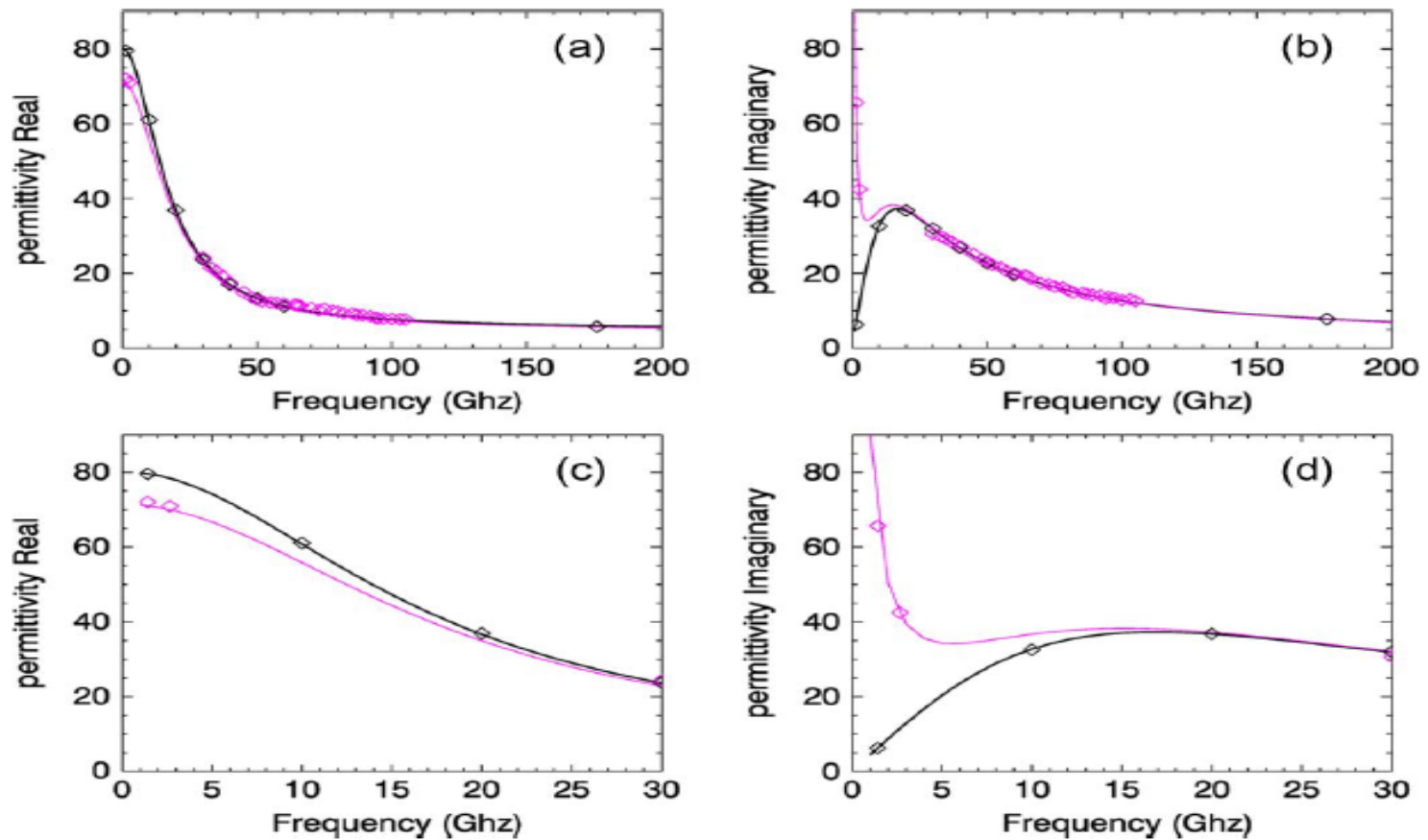
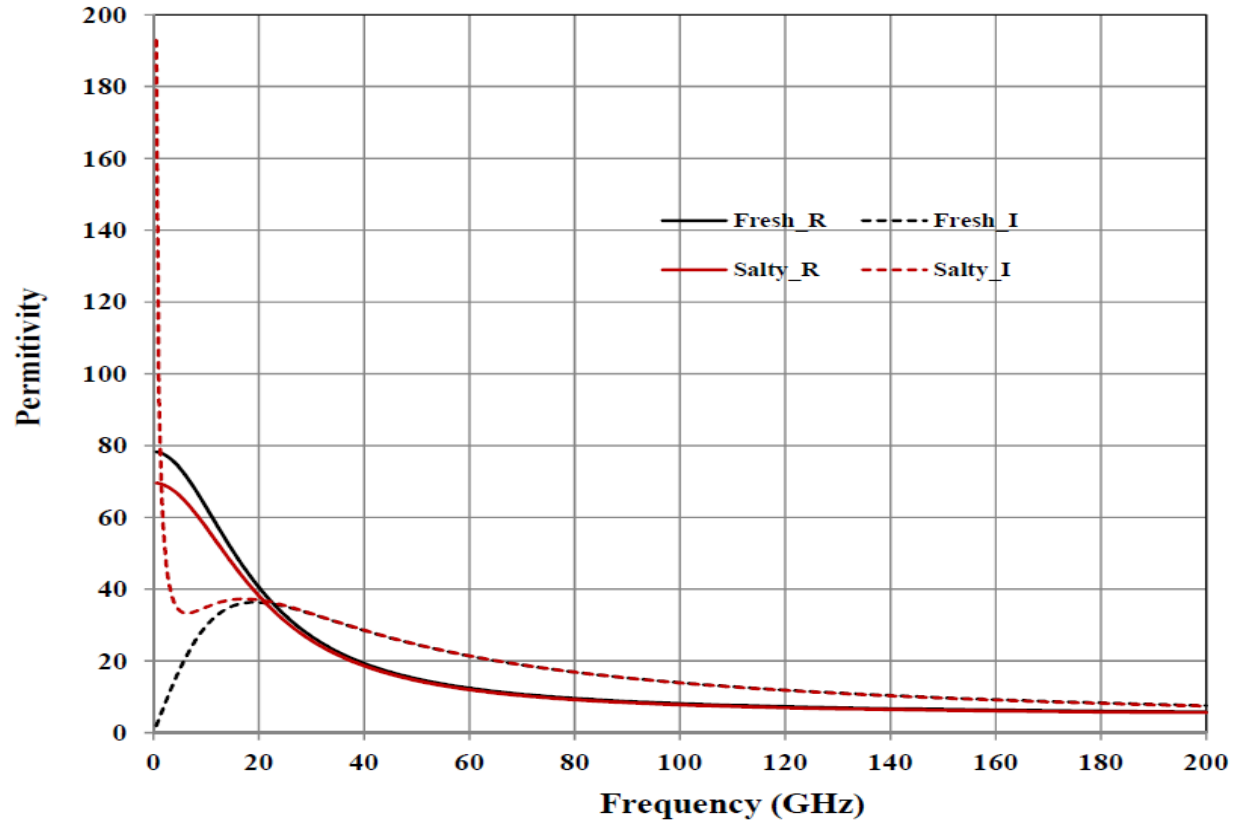


Fig. 1. Panels (a) and (b) represent the real and imaginary parts of the permittivity. Panels (c) and (d) are a zoom-in part for low frequencies. The black line is for fresh water, and the red line is for salt water. The water temperature is 25 °C. The salinity of sea water is 35‰. The solid lines represent the model results. The diamond symbols are for the measurements [12], [14], [18], [20]–[23].

# Water Permittivity vs. Frequency

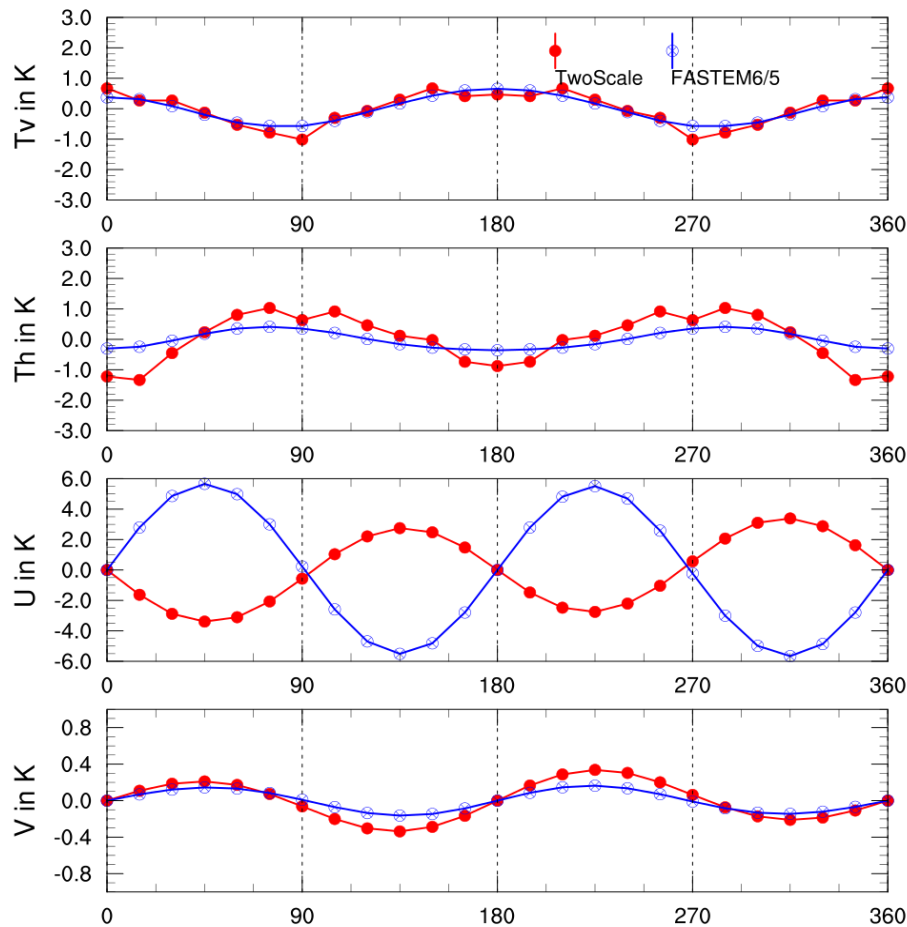


The permittivity model of Ellison (2003) is for a fixed salinity of 35‰. The permittivity model Black line for fresh water and red line for sea water. The symbol squares are measurements for fresh water (black) and sea water (red).



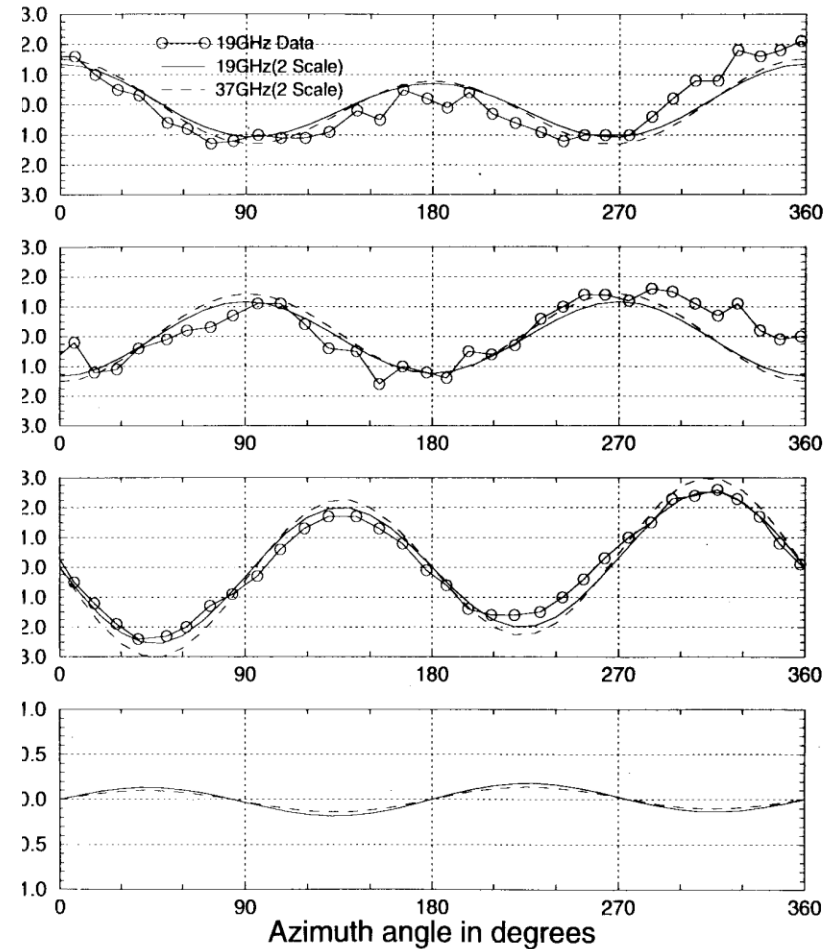
# Comparison of Model Simulations with JPL WINDRAD Observations ( $\theta=30^\circ$ )

## FASTEM6/5 and Two-Scale



## JPL WINDRAD 93 DATA VS. THEORY

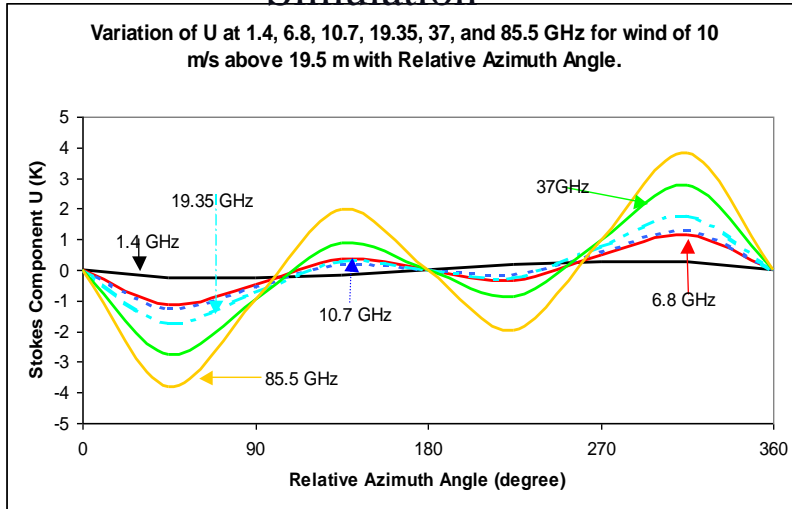
Wind=11m/s@5m;  $\theta=30$  deg



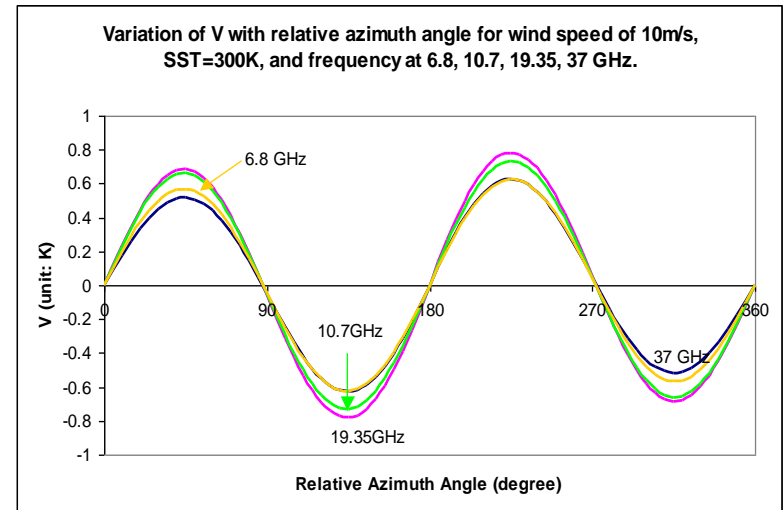
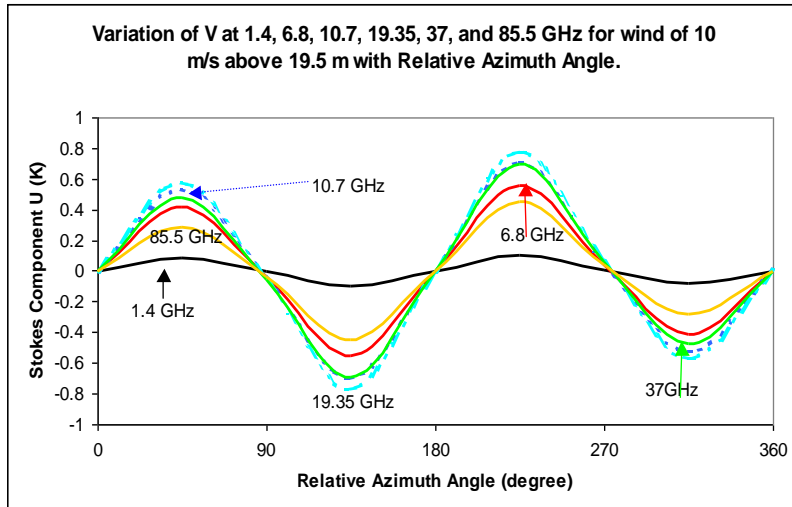
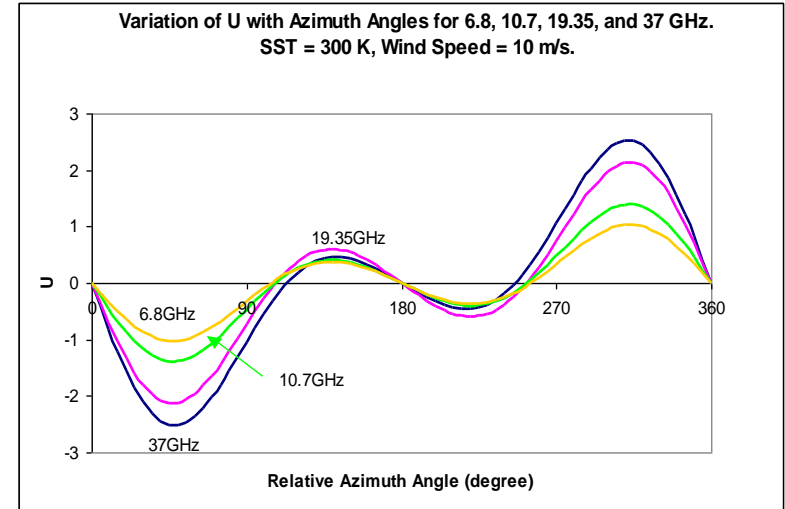
Yueh 1997

# Two-Scale Ocean Emissivity Model vs. NRL Observations

## Simulation

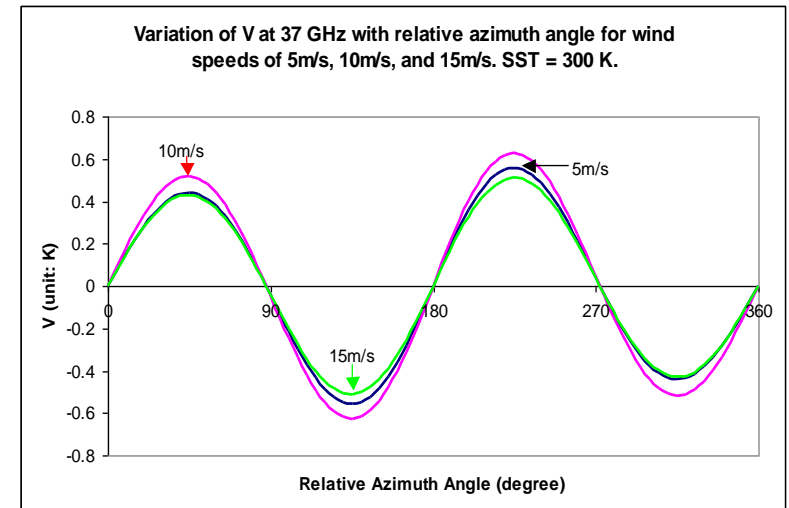
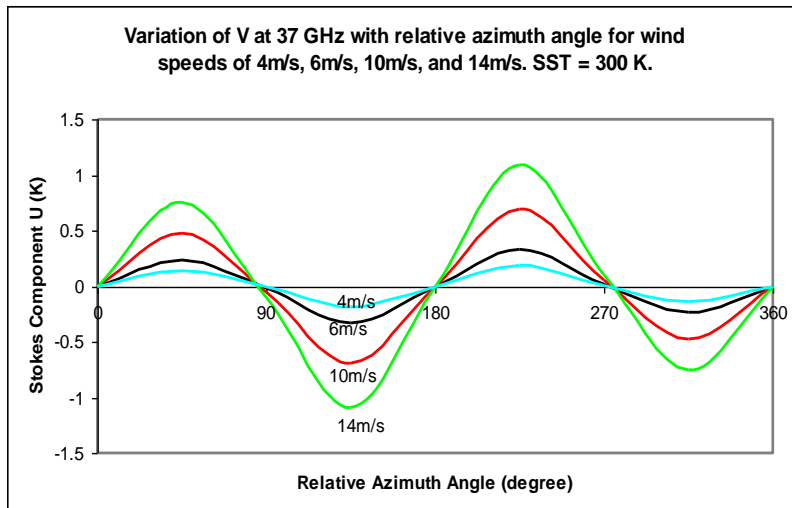
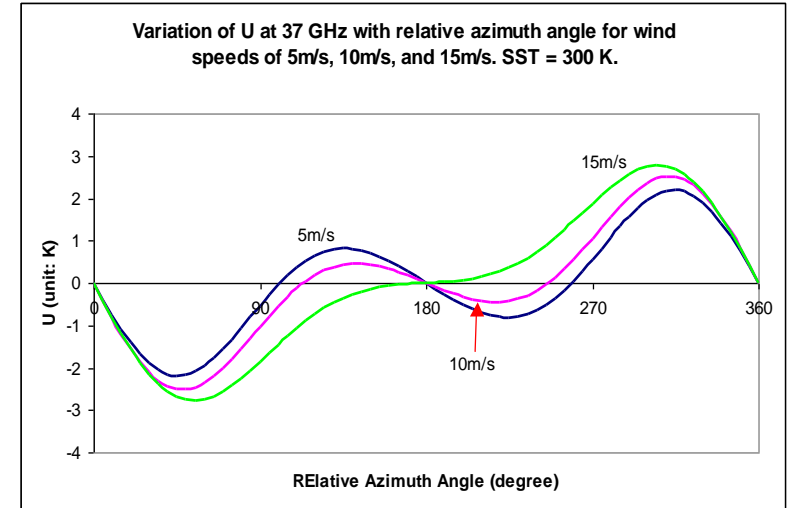
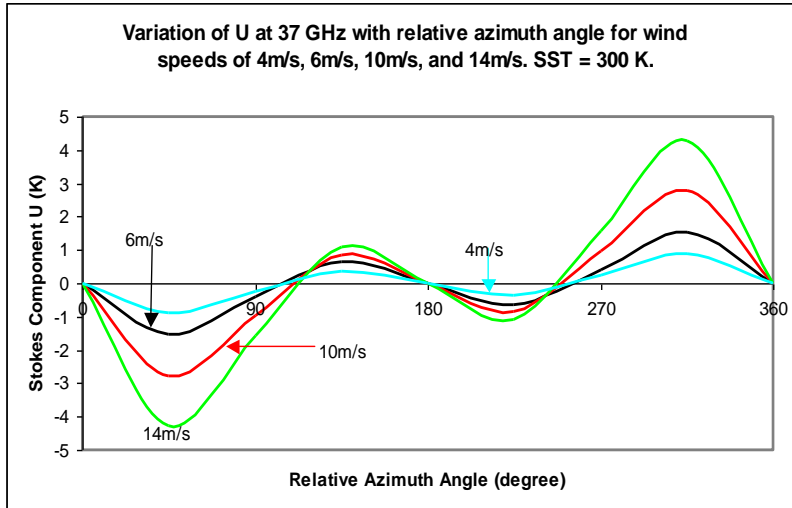


## Measurement

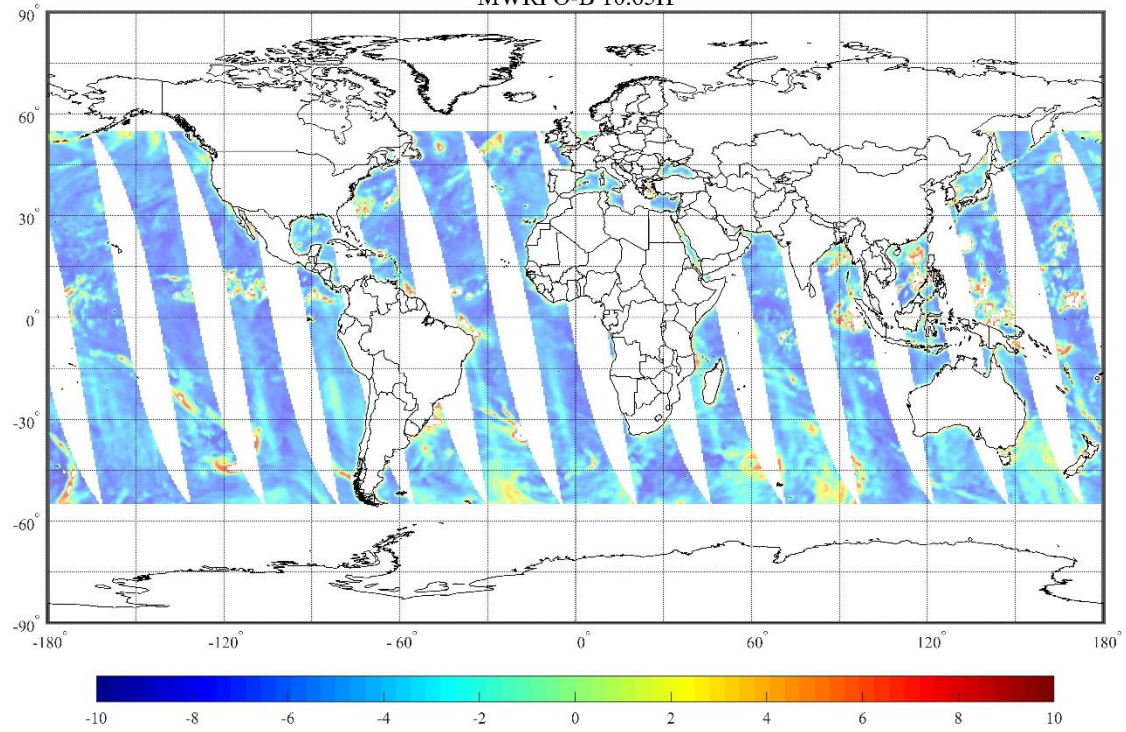


# Two-Scale Ocean Emissivity Model vs. NRL Observations

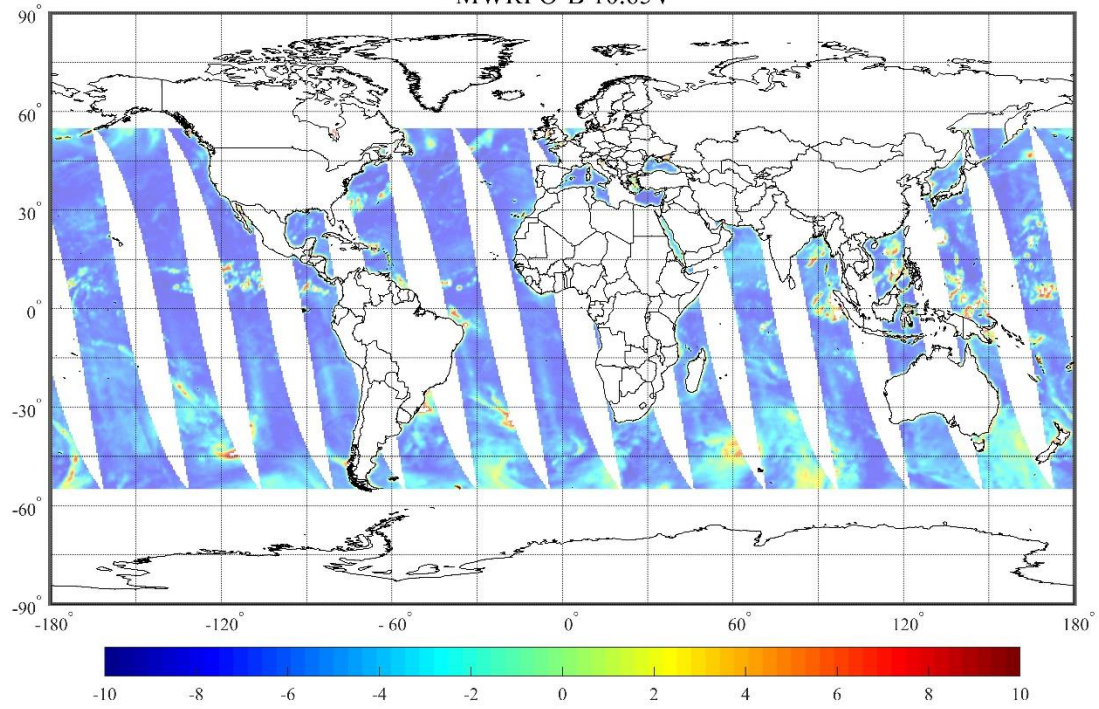
## Simulation

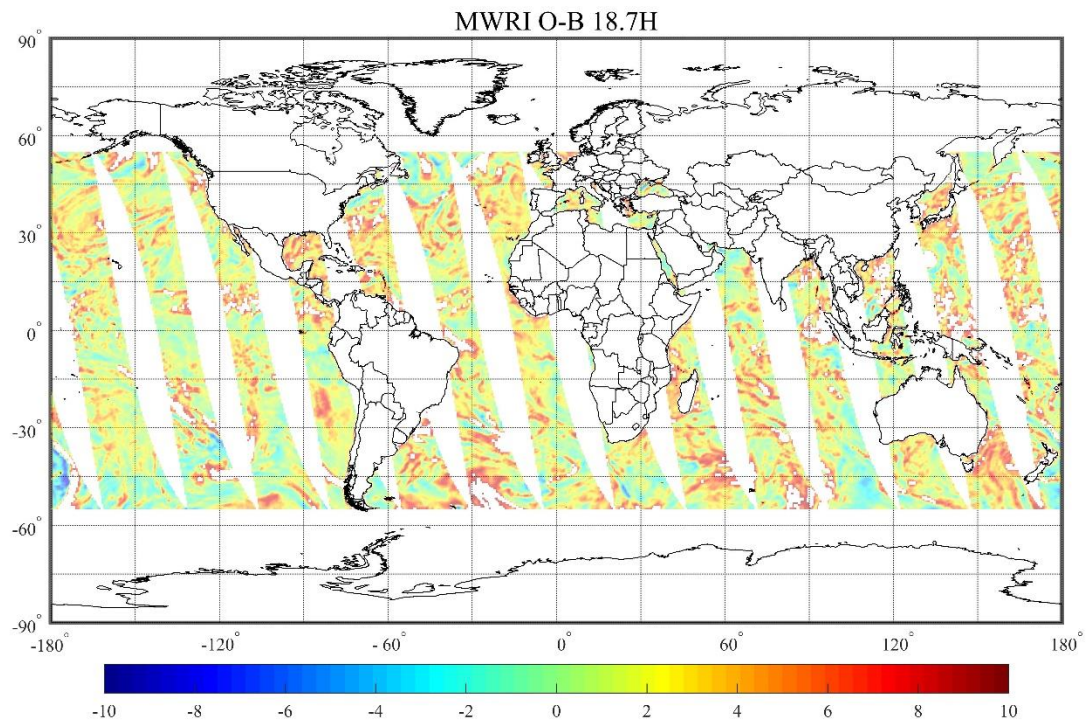


MWRI O-B 10.65H

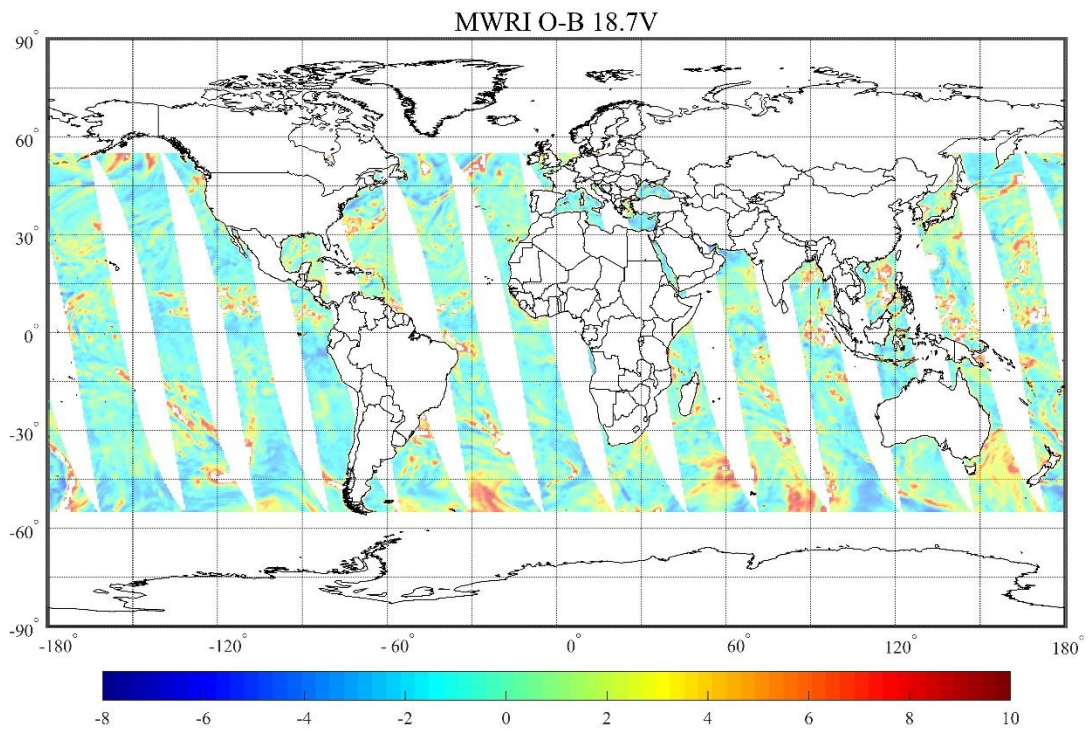


MWRI O-B 10.65V

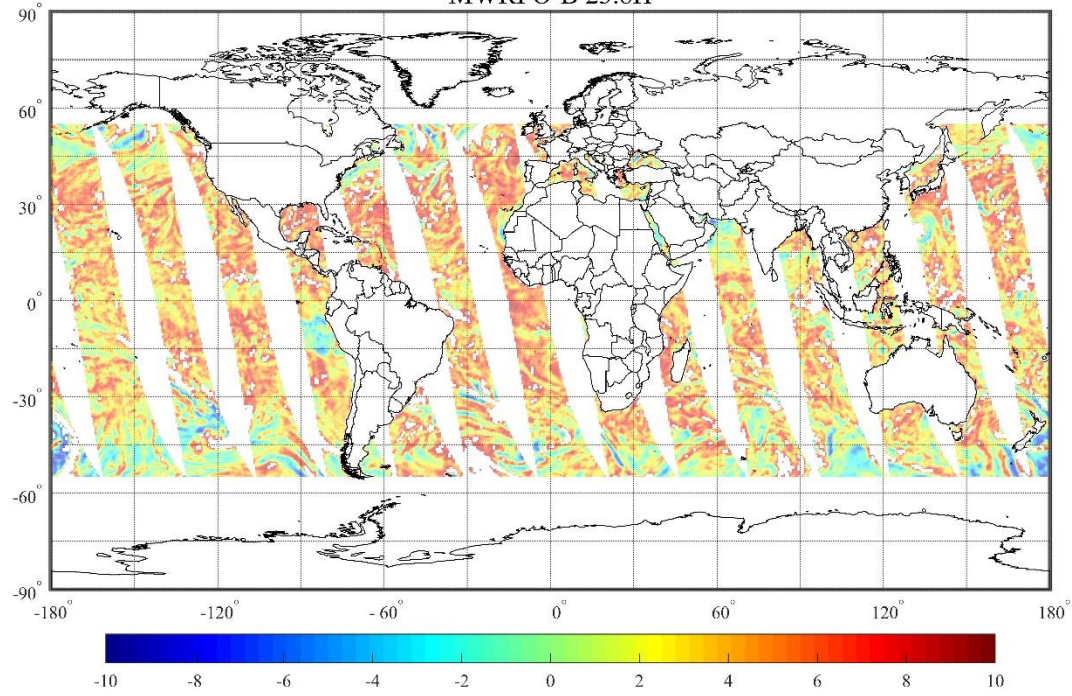




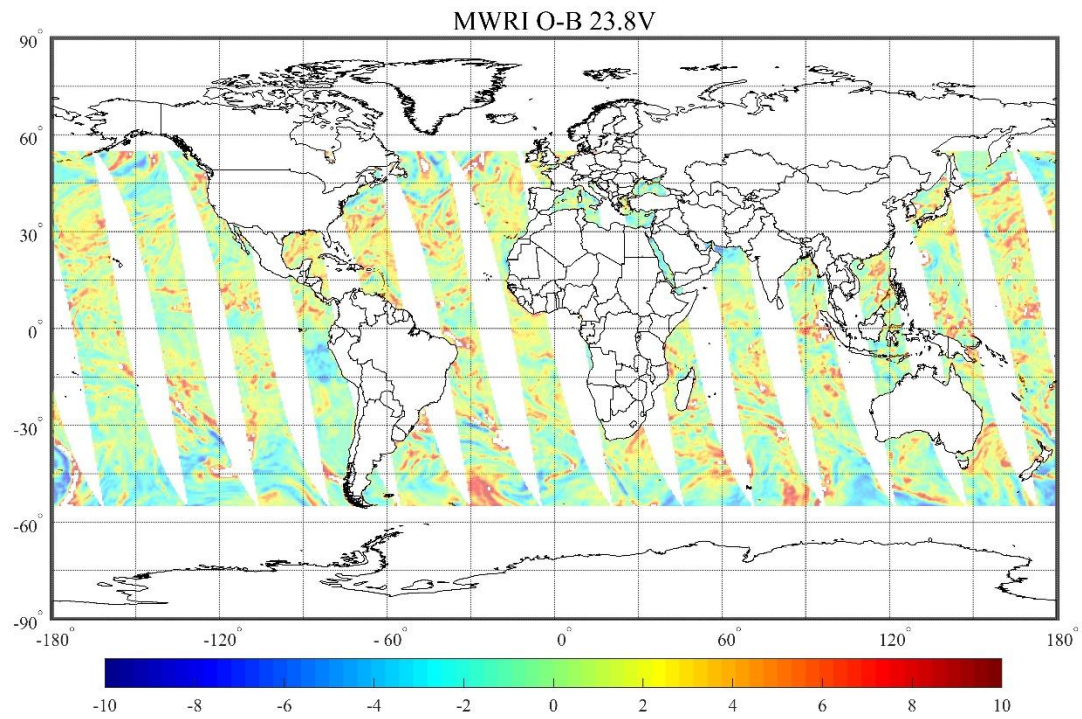


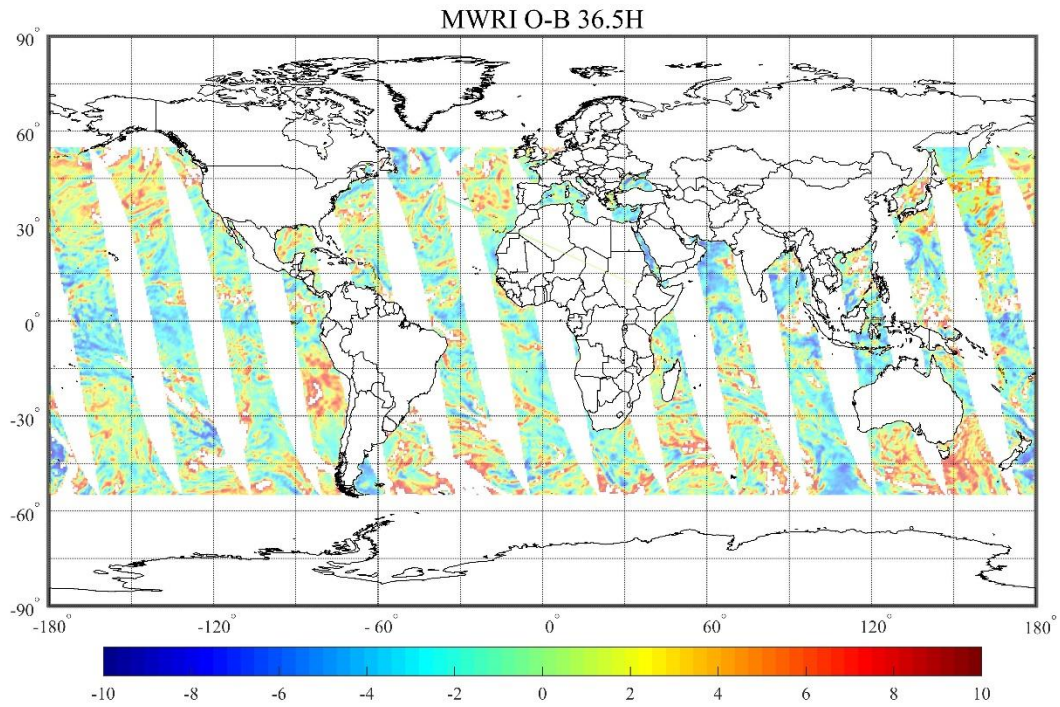


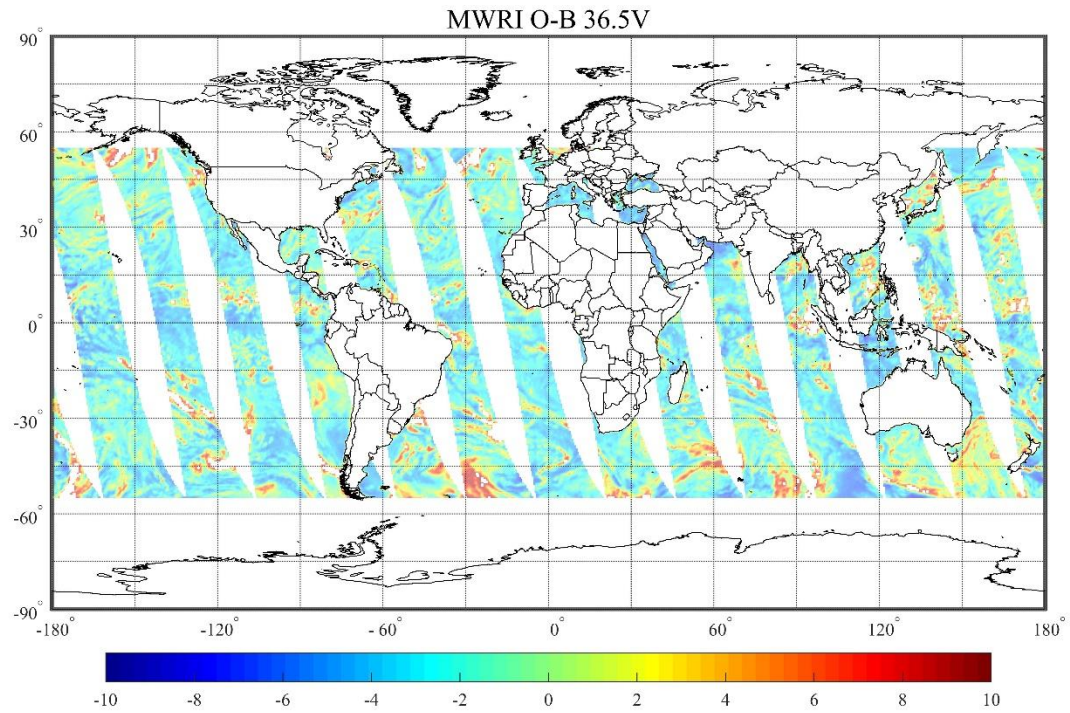
MWRI O-B 23.8H



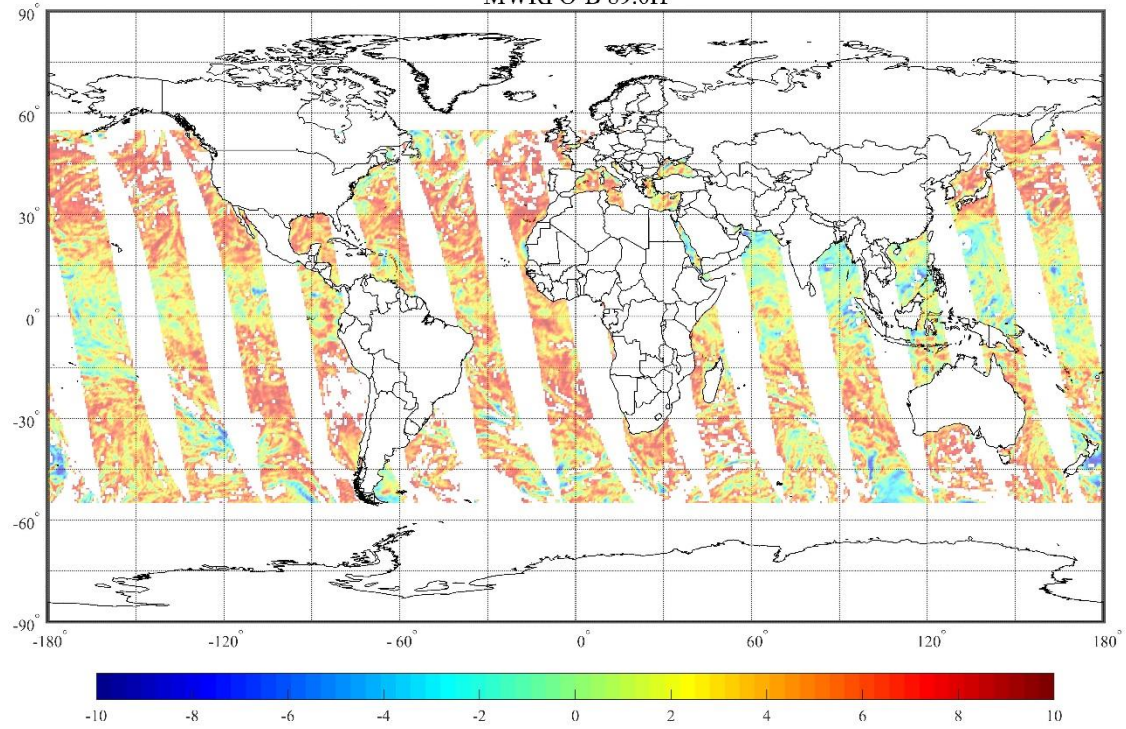






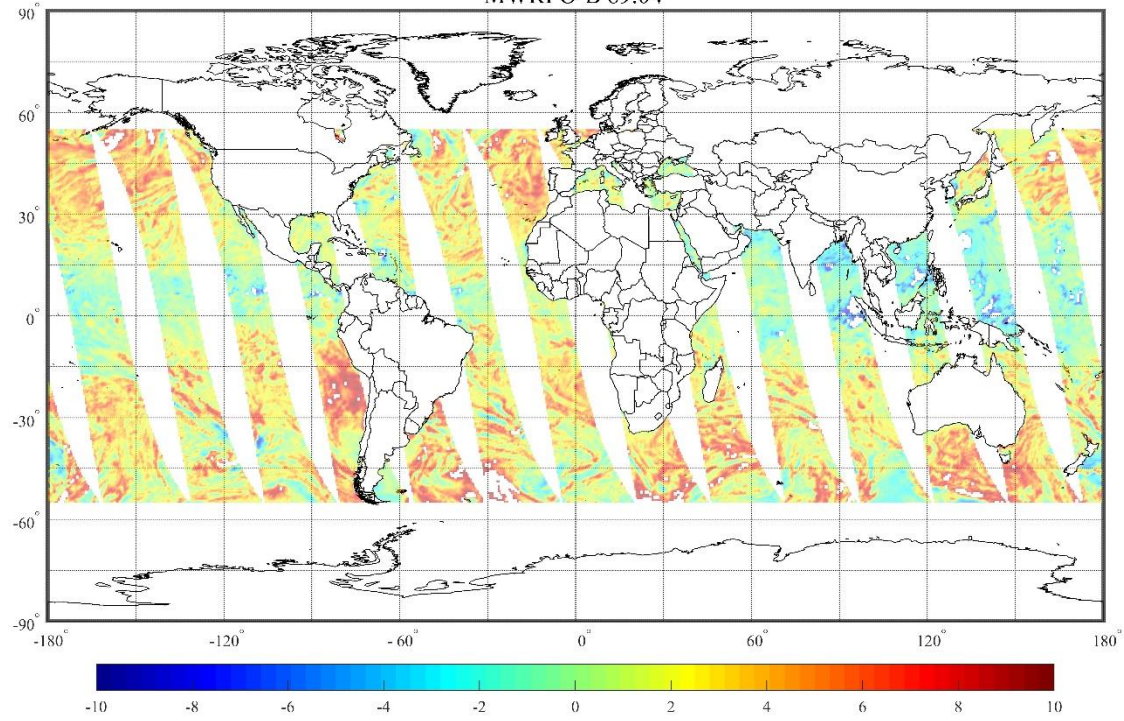


MWRI O-B 89.0H





MWRI O-B 89.0V



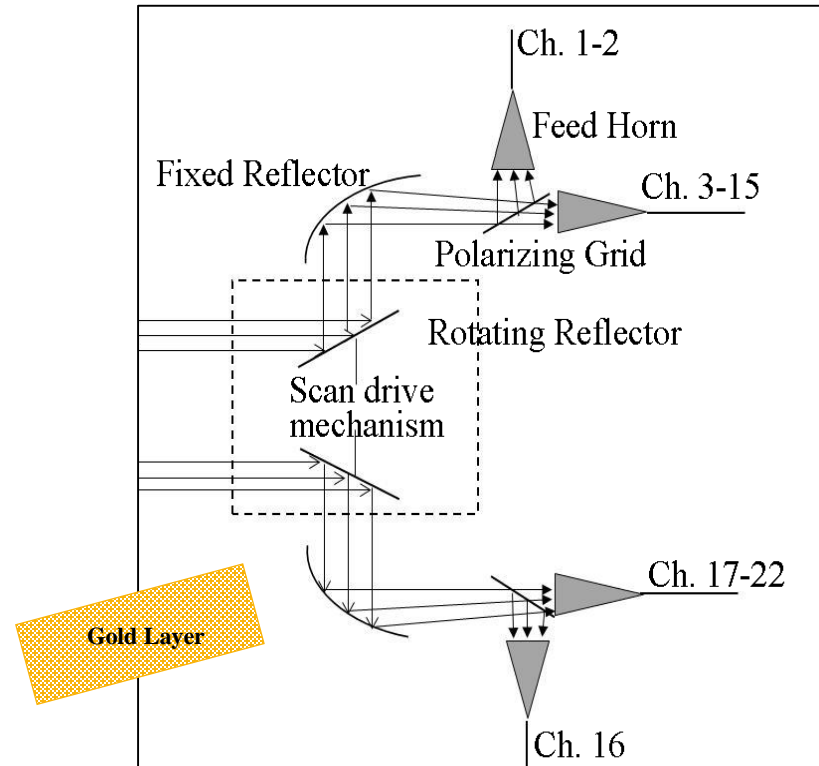
# ATMS Reflector Emission and Its Effects on TDR

- Flat rotating reflector has an emission and affects the accuracy in computing the calibration target temperatures in two point calibration equations
- In the earth scene scanning, the antenna brightness temperature in the two-point calibration equation contains emission that must be further corrected
- Hagen-Rubens equation

$$\varepsilon_N = \sqrt{16\pi e_0 f / \sigma}$$

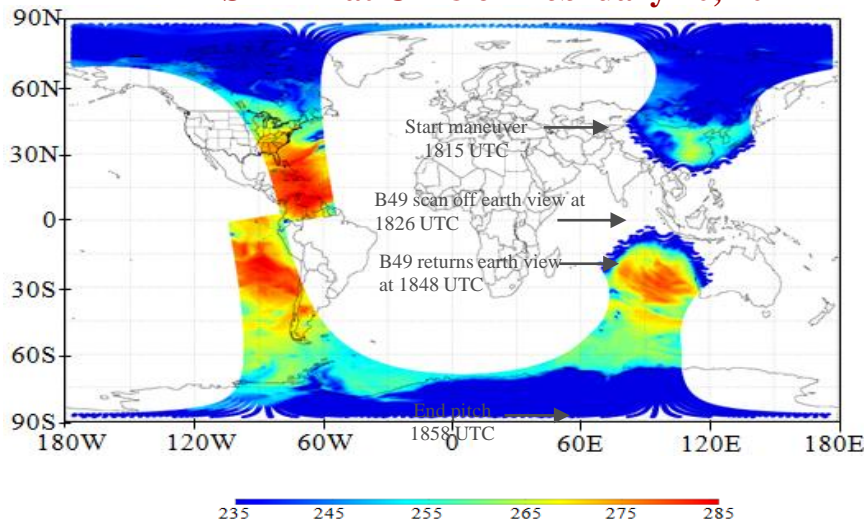
0.0025 to 0.0065

- An algorithm is being developed for ATMS TDR correction

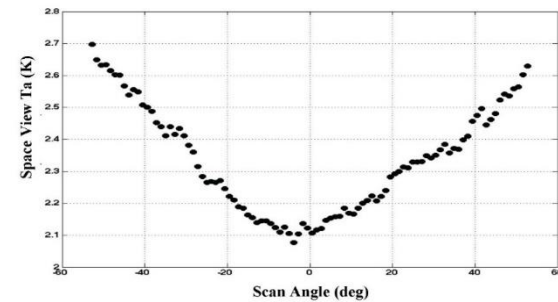


# ATMS TDR Pitch-over Maneuver Data

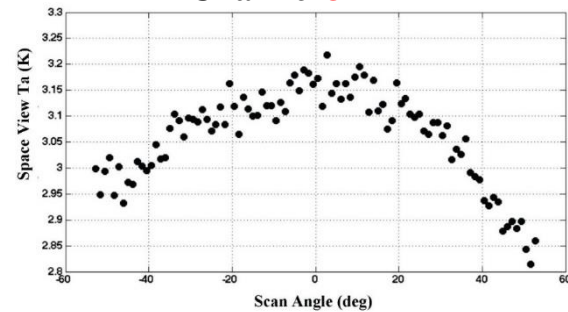
**ATMS TDR at Ch18 on February 20, 2012**



**Channel 1**

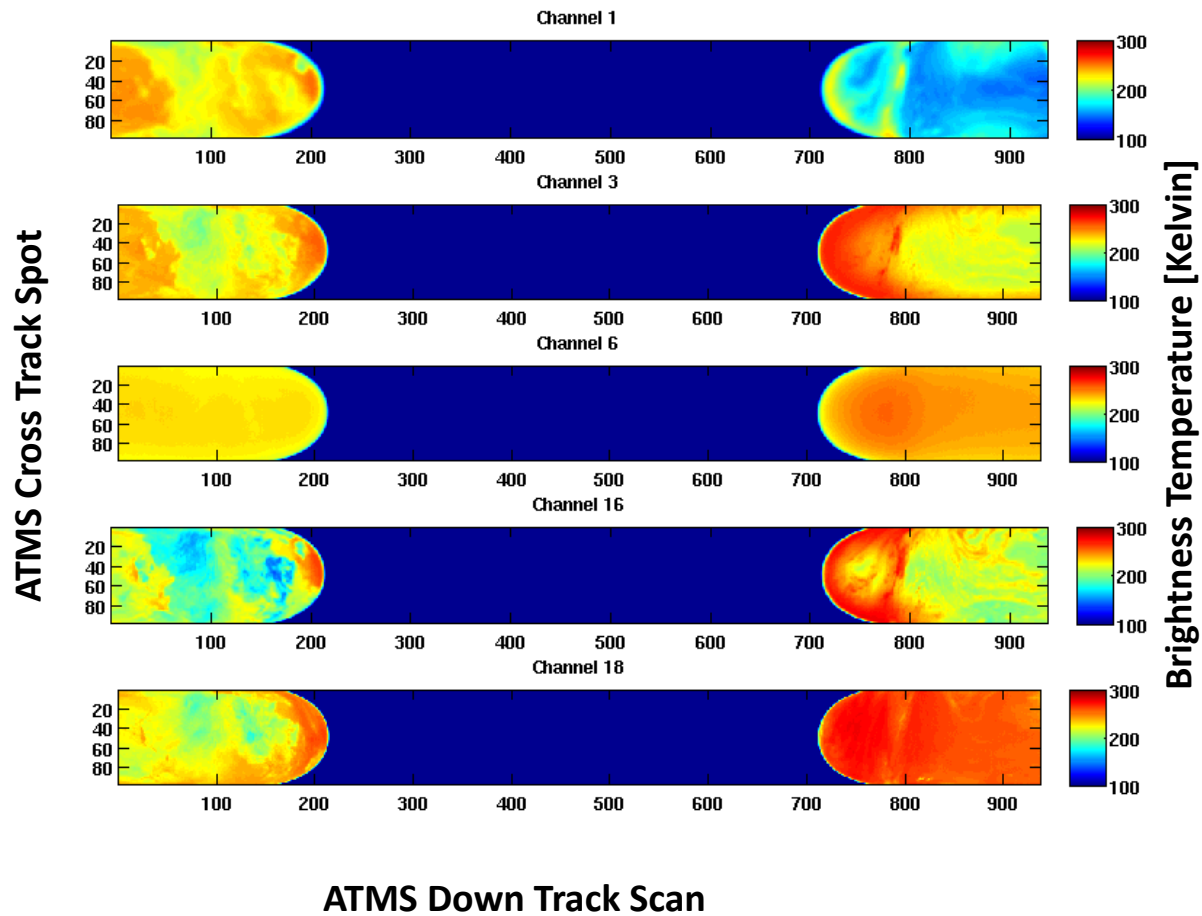


**Channel 3**



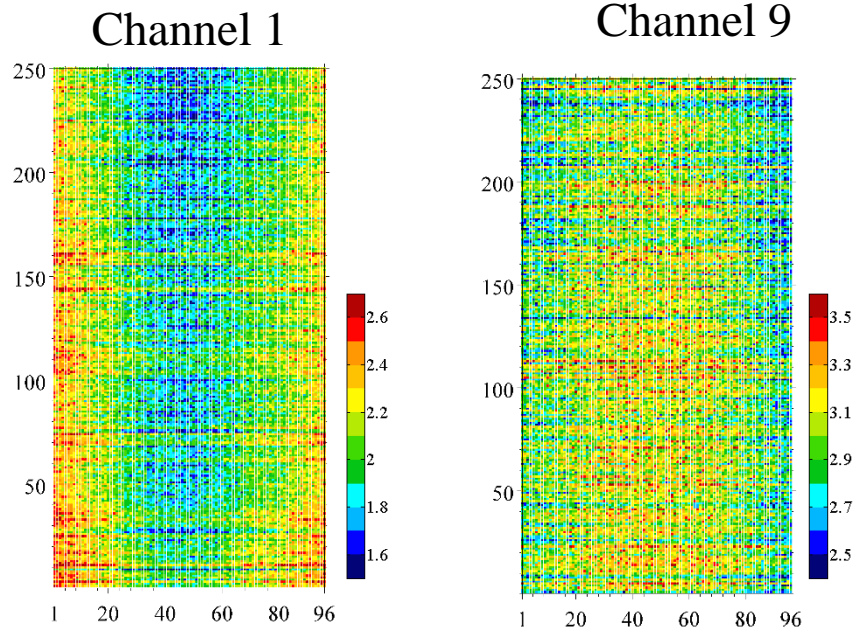
*NPP ATMS pitch maneuver observations show channel related scan angle dependent feature, indicate the scan bias is not inherent feature of the scene*

# SNPP Pitch-Over Maneuver 20 Feb12

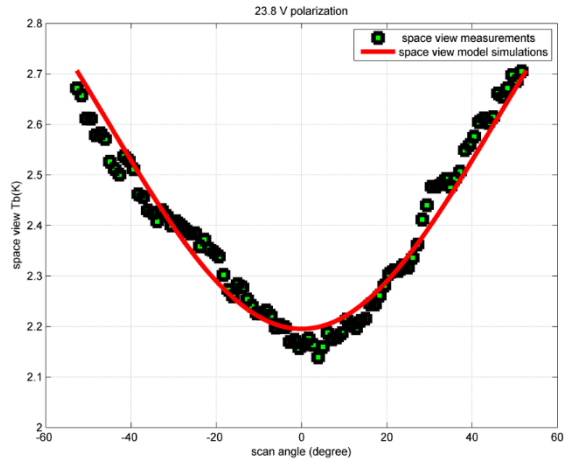




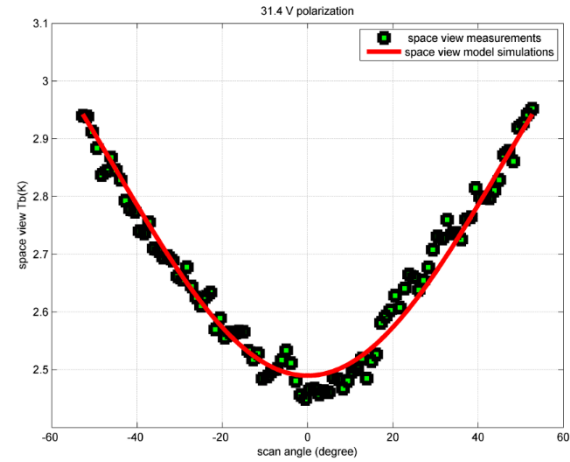
# Pitch-Over Maneuver Data in Details



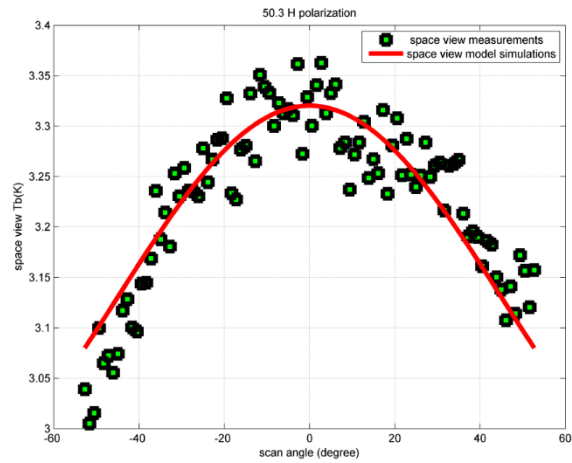
### Channel 1



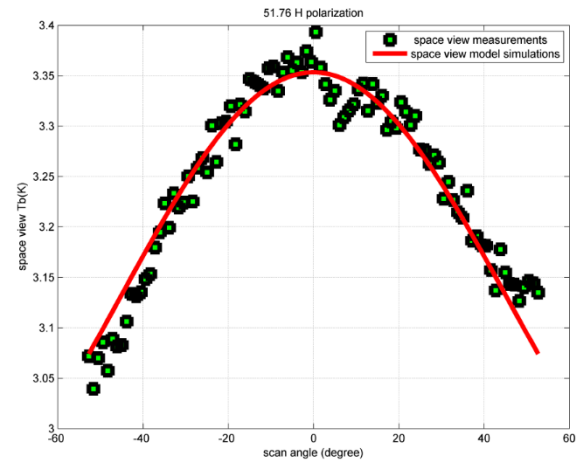
### Channel 2



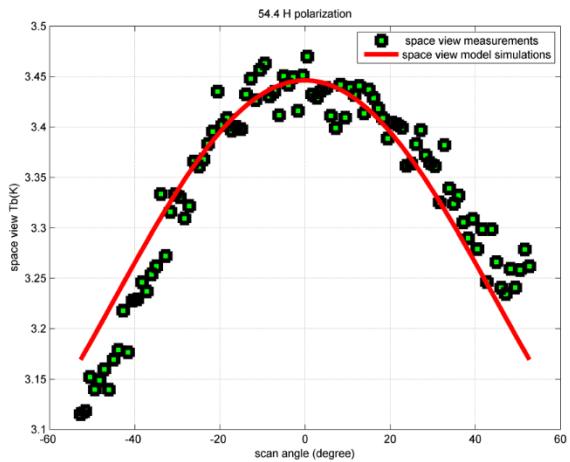
### Channel 3



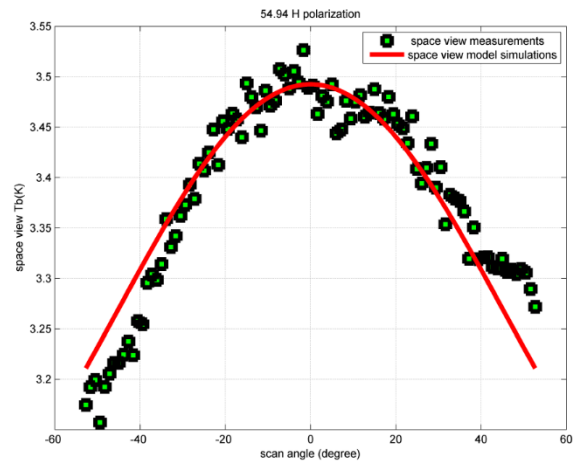
### Channel 4



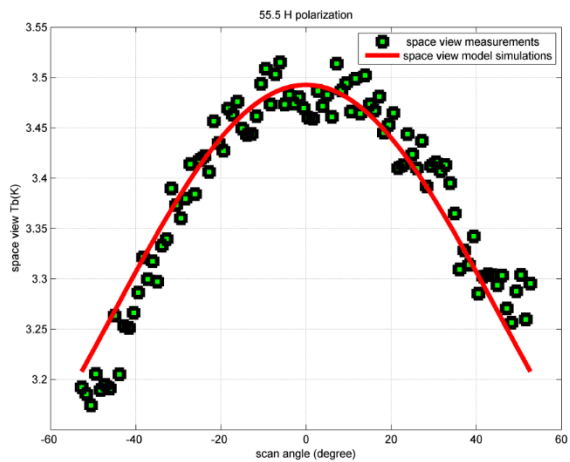
### Channel 5



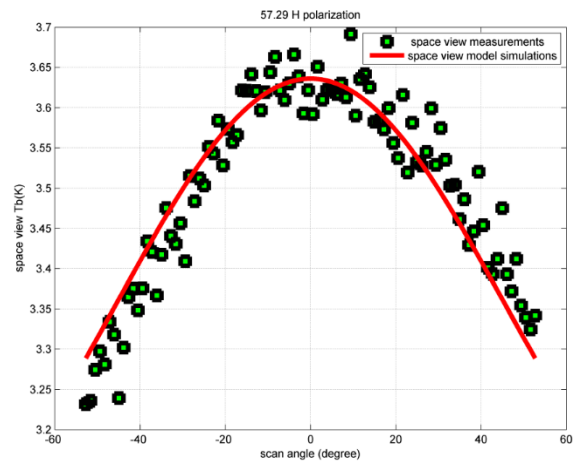
### Channel 6



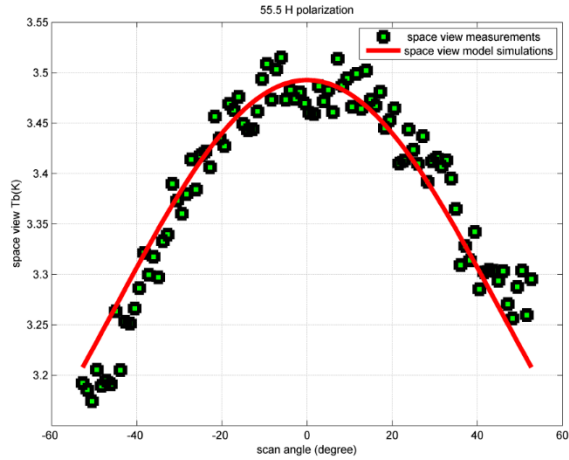
### Channel 7



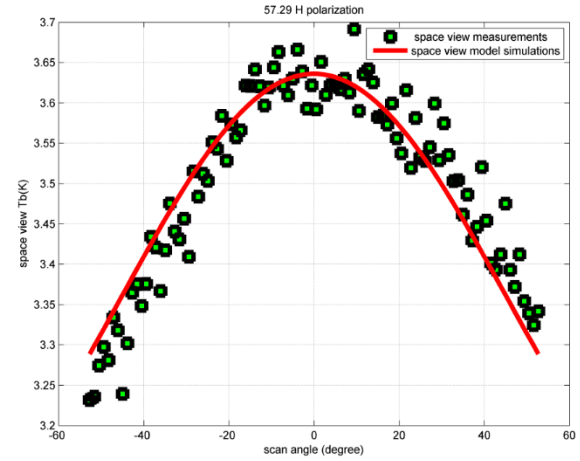
### Channel 8



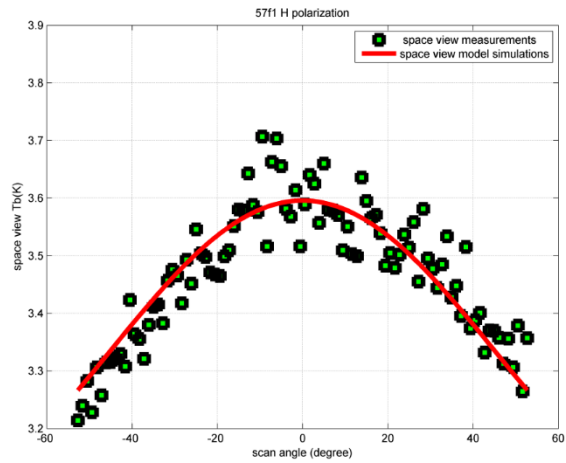
### Channel 9



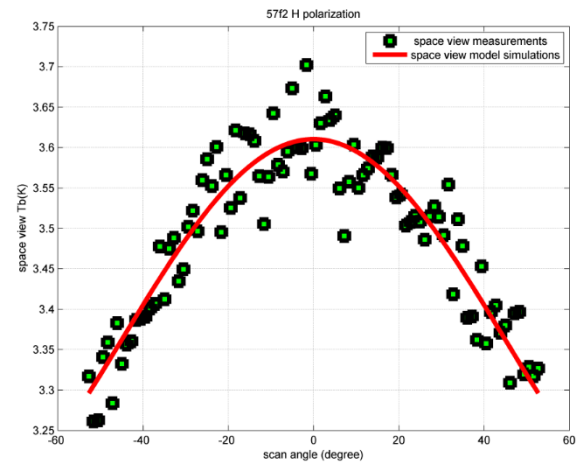
### Channel 10



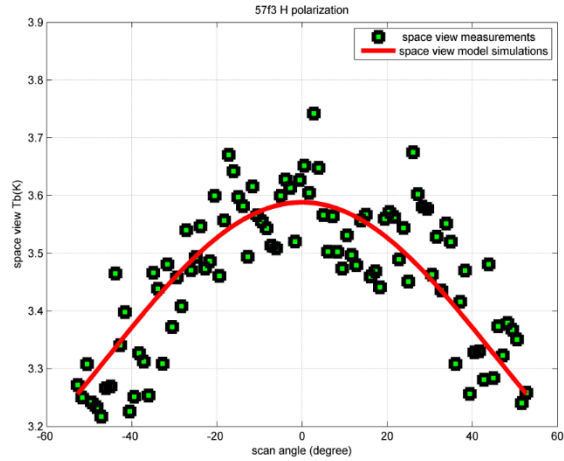
### Channel 11



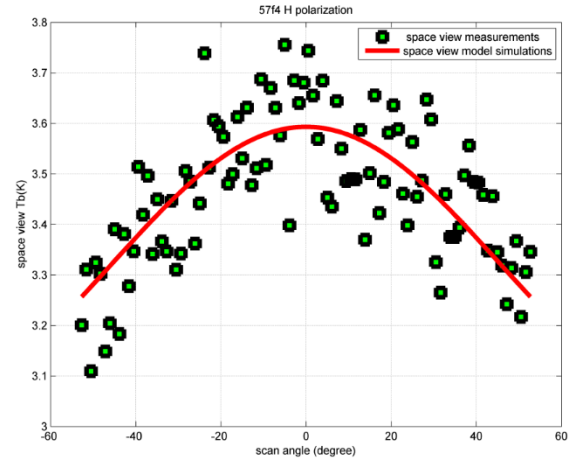
### Channel 12



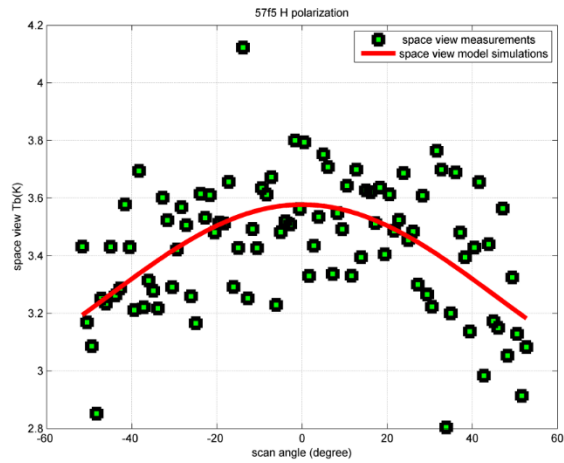
### Channel 13



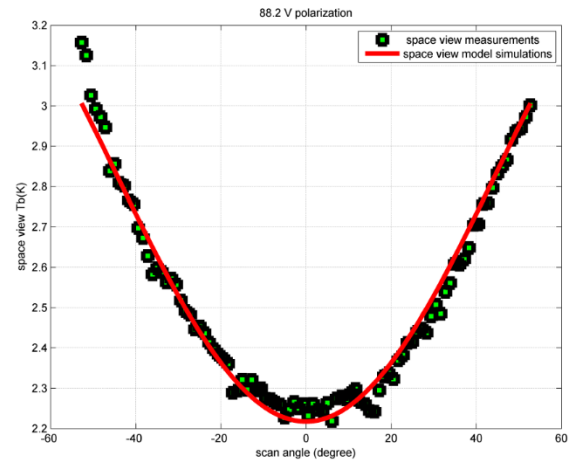
### Channel 14



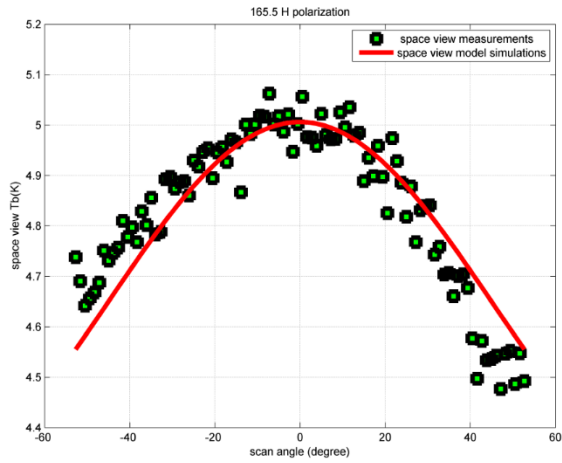
### Channel 15



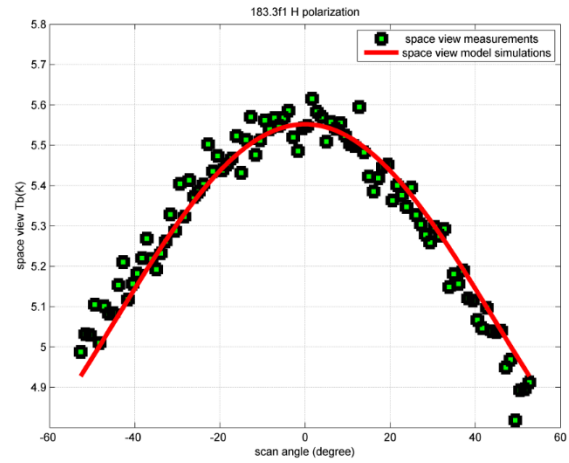
### Channel 16



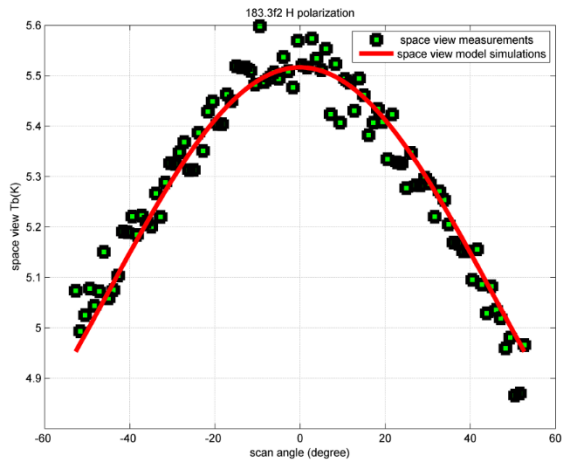
### Channel 17



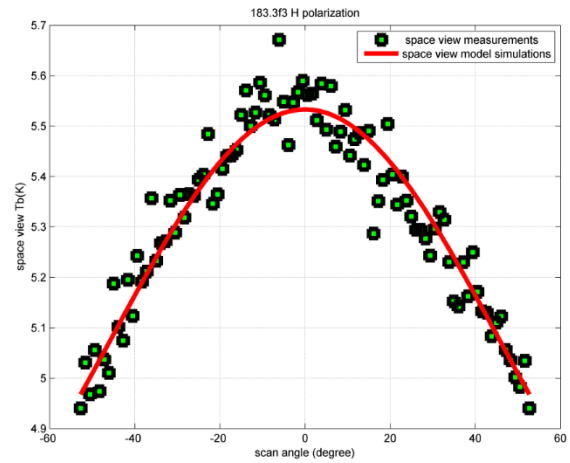
### Channel 18



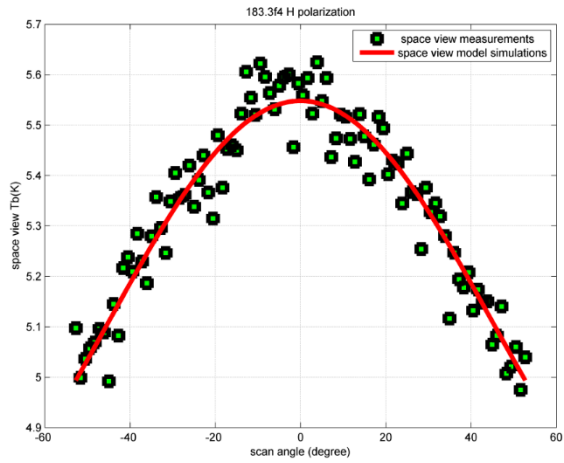
### Channel 19



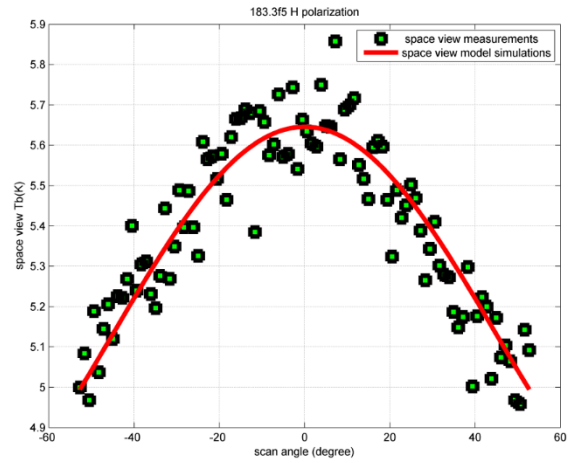
### Channel 20



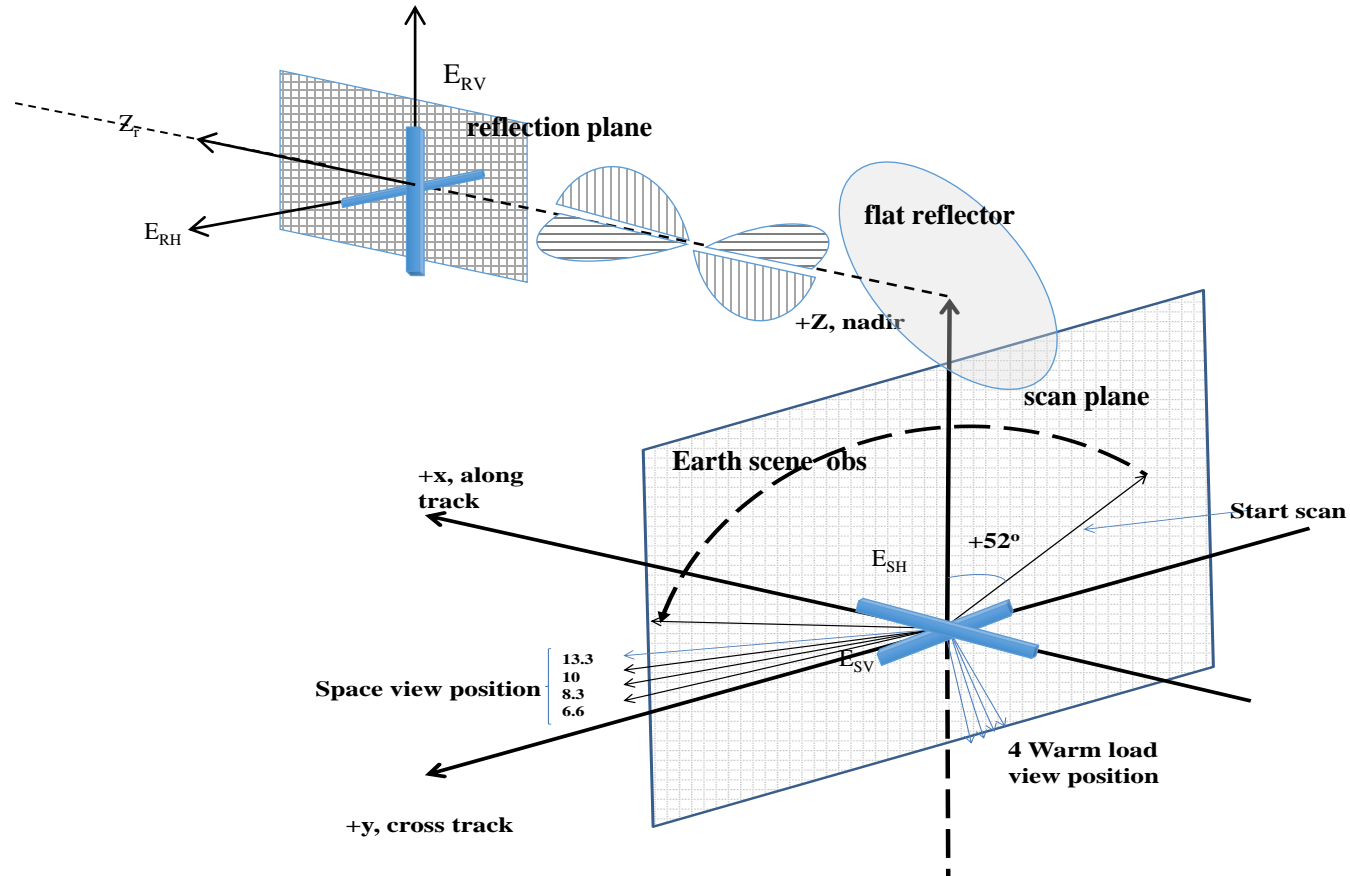
## Channel 21



## Channel 22



# Flat Reflector Emissivity Model





# Effects of ATMS Plane Reflector Emission on TOA Radiances

*For Quasi-V (TDR):*

$$R_{qv}^c = R_{qv} + \varepsilon_h (R_r - R_h) + [\varepsilon_v (R_r - R_v) - \varepsilon_h (R_r - R_h)] \sin^2 \theta - \frac{R_3}{2} (1 - \varepsilon_h)^{3/2} \sin 2\theta$$

*For Quasi-H (TDR):*

$$R_{qh}^c = R_{qh} + \varepsilon_h (R_r - R_h) + [\varepsilon_v (R_r - R_v) - \varepsilon_h (R_r - R_h)] \cos^2 \theta + \frac{R_3}{2} (1 - \varepsilon_h)^{3/2} \sin 2\theta$$

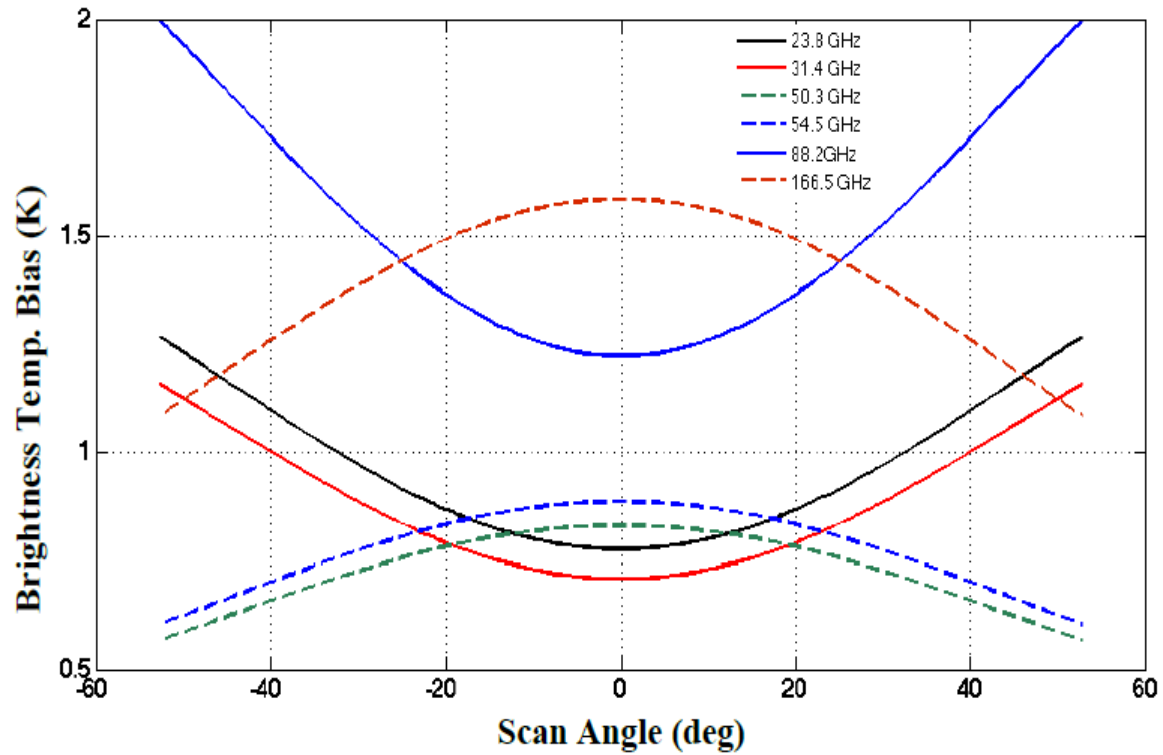
**The second and third terms are the biases related to the reflector emission**

*At an incident angle of 45 degree to the plane reflector, the Fresnel equation becomes*

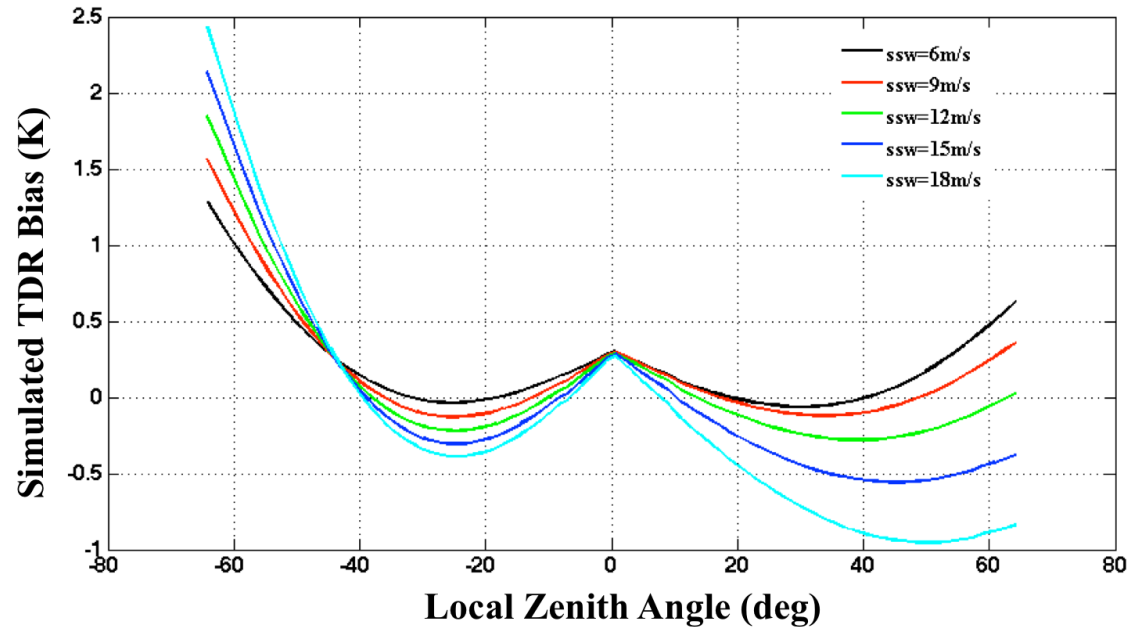
$$\varepsilon_v = 2\varepsilon_h - \varepsilon_h^2$$

*Weng and Yang, 2016, Remote Sensing*

# The Cold Space Bias due to Reflector Emission

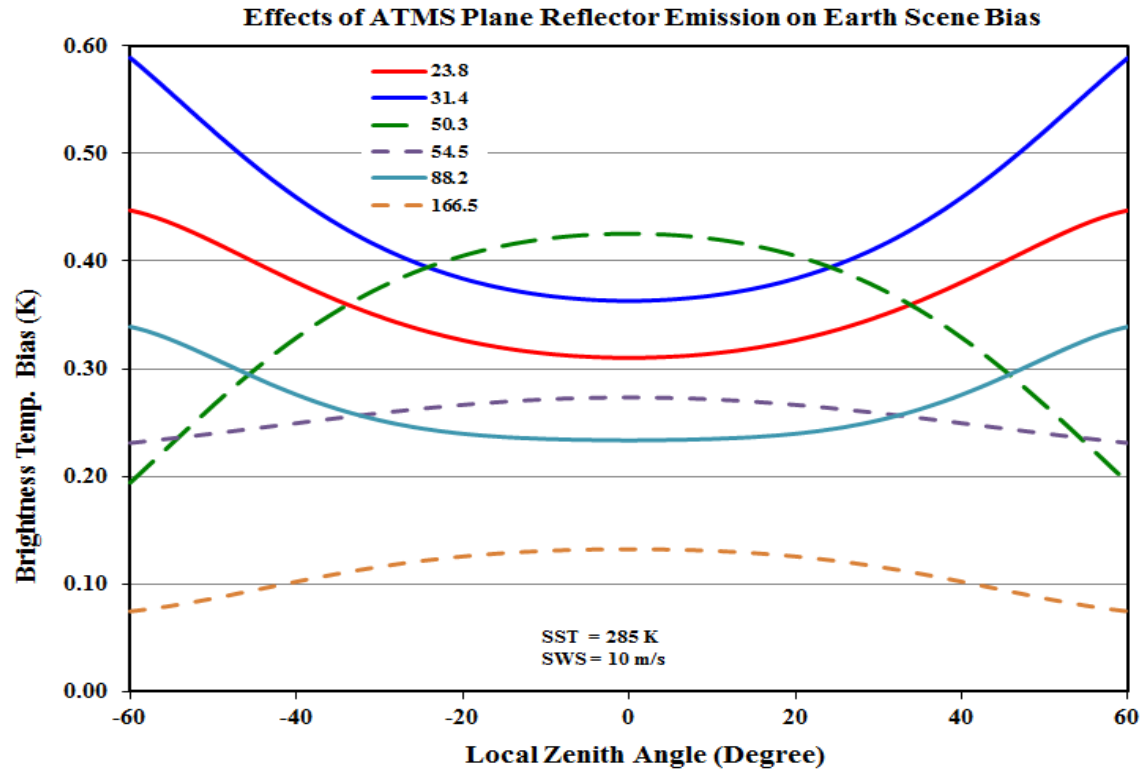


# Radiative Transfer Simulation Including ATMS Reflector Emission

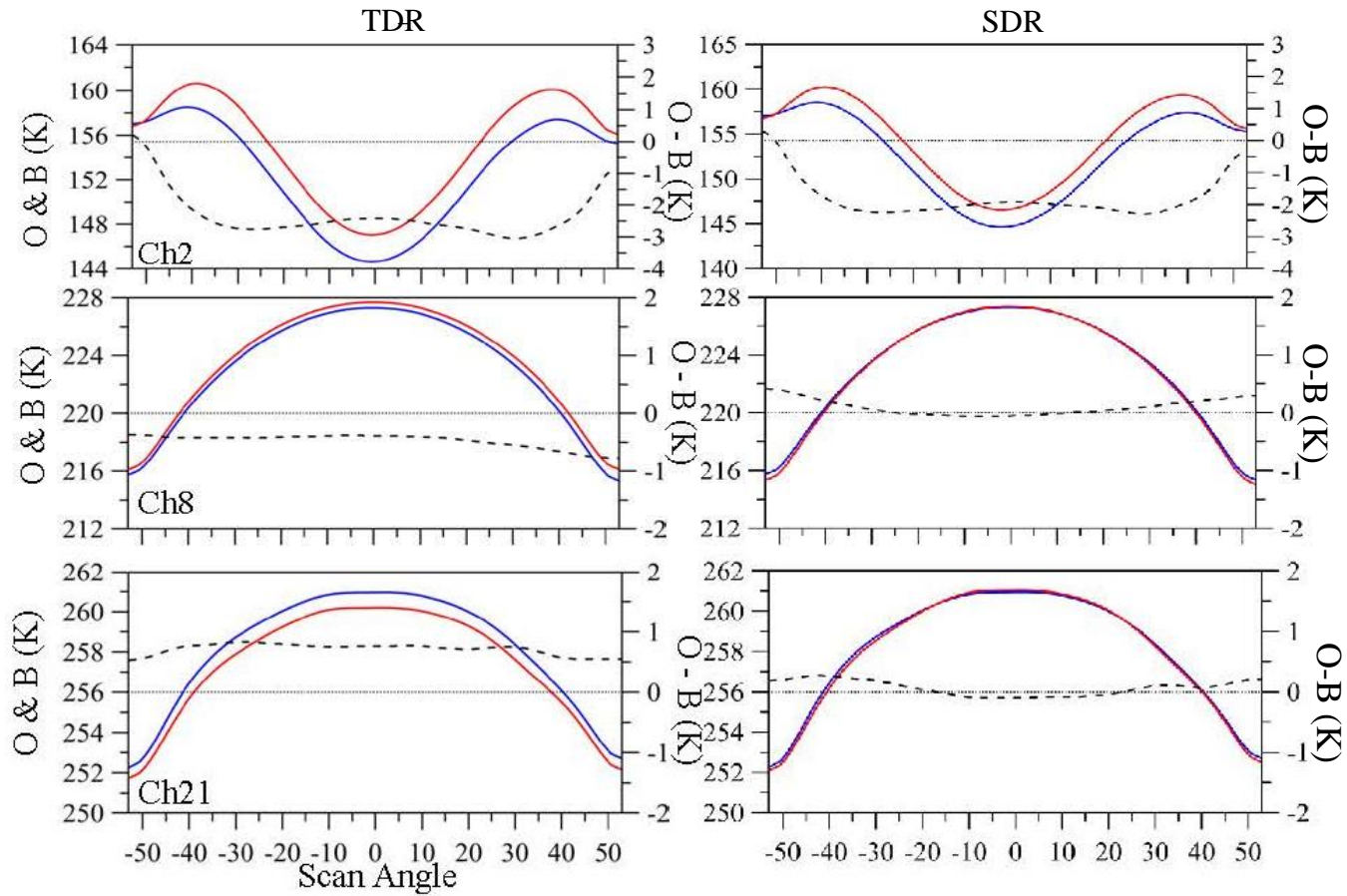


- For polarized scene, the impact of reflector emission is dependent on the temperature difference between antenna reflector and V-pol scene
- The scan angle dependent feature in the error is mainly dominated by the third Stokes component of the scene radiation
- The simulated scan bias in TDR is consistent with those in real observations

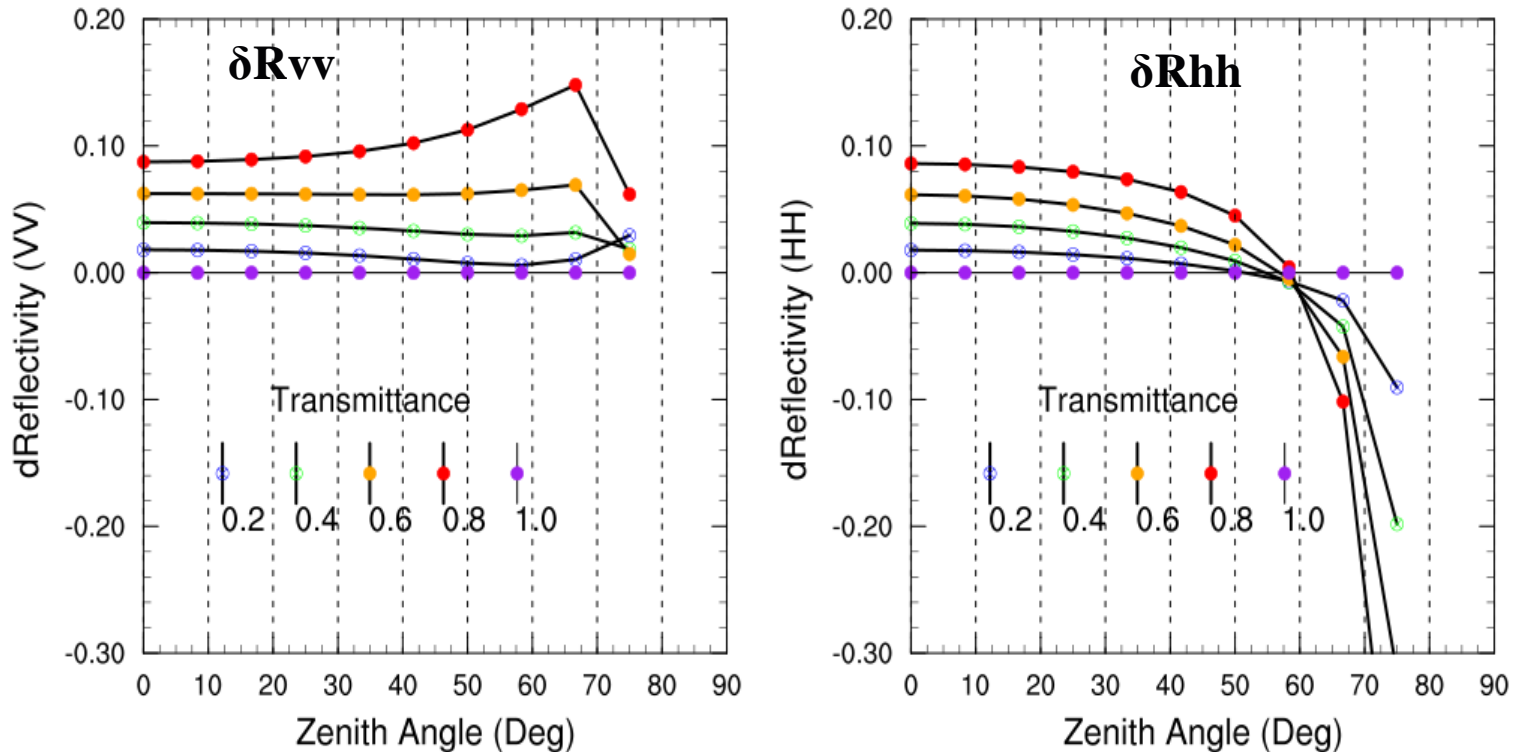
# The Earth Scene Bias due to Reflector Emission



# ATMS Scan Dependent O-B (TDR vs. SDR)



# Reflection Correction in FASTEM6/5



FASTEM reflection correction ( $\delta R(\tau) = R(\tau) - R(\tau=0)$ ) in terms of transmittance appears physically unreasonable. In general, one would expect larger reflection correction in more cloudy cases. FASTEM6/5 shows the opposite way. Correction for zenith  $>60^\circ$  is also problematic.

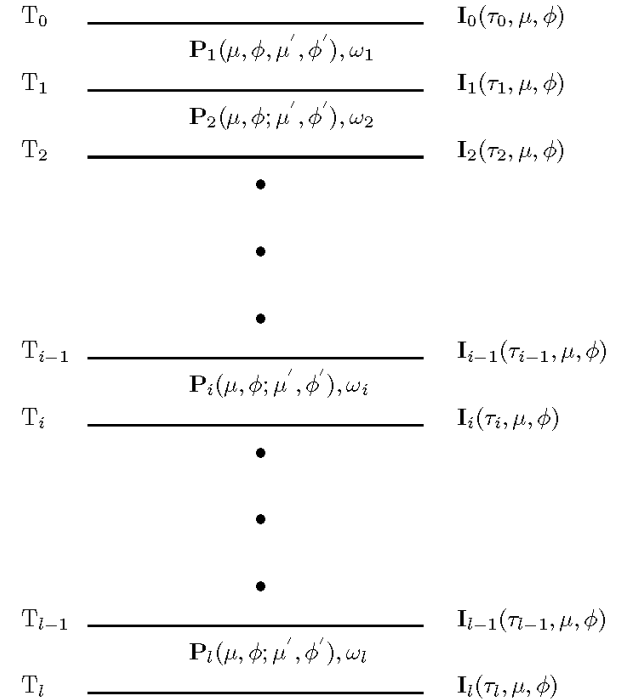
# DISORT and VDISORT Solutions

$$\mathbf{I} = \exp[\mathbf{A}(\tau - \tau_{l-1})]\mathbf{C}_1 + \mathbf{S}_1$$

$$\begin{aligned} \mathbf{S}_1 = & \delta_{m_0} \{ B(\tau_{l-1})\Xi + \frac{B(\tau_{l-1}) - B(\tau_l)}{\tau_{l-1} - \tau_l} [\mathbf{A}_l^{-1}\Xi + (\tau - \tau_{l-1})\Xi] \\ & + \mu_0 [\mu_0 \mathbf{A}_l + \mathbf{E}]^{-1} \frac{\omega F_0}{\pi} \exp(-\tau / \mu_0) \Psi \} \end{aligned}$$

$$\mathbf{I}_1(0) = \mathbf{I}_0$$

$$\mathbf{I}_1(\tau_{l-1}) = \mathbf{I}_{1-1}(\tau_{l-1})$$



$$\mathbf{I}_L(\tau_L) = \varepsilon B(T_s) + \mathbf{R}\mathbf{I}_L(\tau_L) + \mathbf{R}_0 \frac{F_0}{\pi} \exp(-\tau_L / \mu_0) \Xi$$

# Summary and Conclusions

- The two-scale model has been used for training the fastem coefficients and produces the simulations in azimuth direction similar to the measurements.
- The 3<sup>rd</sup> and 4<sup>th</sup> Stokes emissivity from current FASTEM have a phase shift in azimuth direction. Some fix is required if it is used for a full polarimetric simulation
- FY MWRI simulations from using FASTEM have larger biases and the biases may be most likely caused by the instrument design and calibration uncertainty
- The correction to the fastem emissivity from atmospheric downwelling is a little bit odd.